9

Corrosion Fatigue Behaviour of Aluminium 5083-H111 Welded Using Gas Metal Arc Welding Method

Kalenda Mutombo[1] and Madeleine du Toit[2]
[1]*CSIR/*
[2]*University of Pretoria*
South Africa

1. Introduction

Aluminium and its alloys are widely used as engineering materials on account of their low density, high strength-to-weight ratios, excellent formability and good corrosion resistance in many environments. This investigation focused on one popular wrought aluminium alloy, namely magnesium-alloyed 5083 (in the strain hardened -H111 temper state).

Aluminium alloy 5083 is one of the highest strength non-heat treatable aluminium alloys, with excellent corrosion resistance, good weldability and reduced sensitivity to hot cracking when welded with near-matching magnesium-alloyed filler metal. This alloy finds applications in ship building, automobile and aircraft structures, tank containers, unfired welded pressure vessels, cryogenic applications, transmission towers, drilling rigs, transportation equipment, missile components and armour plates. In many of these applications welded structures of aluminium are exposed to aqueous environments throughout their lifetimes.

Welding is known to introduce tensile residual stresses, to promote grain growth, recrystallization and softening in the heat-affected zone, and to cause weld defects that act as stress concentrations and preferential fatigue crack initiation sites. Fatigue studies also emphasised the role of precipitates, second phase particles and inclusions in initiating fatigue cracks. When simultaneously subjected to a corrosive environment and dynamic loading, the fatigue properties are often adversely affected and even alloys with good corrosion resistance may fail prematurely under conditions promoting fatigue failure.

The good corrosion resistance of the aluminium alloys is attributed to the spontaneous formation of a thin, compact and adherent aluminium oxide film on the surface on exposure to water or air. This hydrated aluminium oxide layer may, however, dissolve in some chemical solutions, such as strong acids or alkaline solutions. Damage to this passive layer in chloride-containing environments (such as sea water or NaCl solutions), may result in localised corrosive attack such as pitting corrosion. The presence of corrosion pits affects the fatigue properties of the aluminium alloys by creating sharp surface stress concentrations which promote fatigue crack initiation. In welded structures, pits are often associated with coarse second phase particles or welding defects [1-4].

A review of available literature on the corrosion fatigue properties of aluminium 5083 welds revealed limited information. Although the mechanical properties, corrosion behaviour and fatigue properties of this alloy have been studied in depth, the influence of filler wire composition and weld geometry on the fatigue behaviour of fully automatic and semi-automatic welds, and the behaviour of weld joints when simultaneously subjected to a chloride-containing corrosive environment and fatigue loading, have not been investigated in any detail.

This investigation therefore aimed at studying the mechanical properties and corrosion fatigue performance of 5083-H111 aluminium welded using semi-automatic and fully automatic pulsed gas metal arc welding, and ER4043, ER5183 and ER5356 filler wires. The influence of the weld metal and heat-affected zone, weld defects and the weld geometry on the mechanical properties and corrosion fatigue resistance was evaluated. The project also determined the fatigue damage ratio (the ratio of the fatigue life in a NaCl solution to the fatigue life in air) by comparing the S-N curves measured in NaCl and in air for 5083-H111 aluminium in the as-supplied and as-welded conditions.

The background section reviews the relevant literature on the welding of 5083 alloy, their corrosion behaviour in chloride-containing solution, mechanical properties and fatigue behaviour. The research methodology describes experimental procedure followed to characterise the microstructure, their mechanical properties, corrosion behaviour and fatigue properties (in air and in a 3.5% NaCl solution) of 5083-H111 in the as-supplied and as-welded conditions. The results obtained, including weld metal microstructures, hardness profiles, tensile properties, fatigue performance, corrosion behaviour and corrosion fatigue properties in NaCl, are also discussed. Finally, conclusions and recommendations regarding the corrosion fatigue performance of 5083-H111 aluminium alloy welds are provided.

2. Background

Aluminium and its alloys represent an important family of light-weight and corrosion resistant engineering materials. Pure aluminium has a density of only 2.70 g/cm^3, as a result, certain aluminium alloys have better strength-to-weight ratios than high-strength steels. One of the most important characteristics of aluminium is its good formability, machinability and workability. It displays excellent thermal and electrical conductivity, and is non-magnetic, non-sparking and non-toxic.

2.1 Aluminium alloy investigated

Aluminium alloys can be broadly divided into those that are hardenable through strain hardening only, and those that respond to precipitation hardening. Aluminium alloys with the number "5" as first digit in the alloy designation are alloyed with magnesium as primary alloying element. Most commercial wrought alloys in this group contain less than 5% magnesium. A typical chemical composition of such alloy is shown in Table 1.

Alloy	*Al*	*Mg*	*Mn*	*Fe*	*Si*	*Cr*	*Cu*	*Zn*	*Ti*
5083	Balance	4.0-4.9	0.4-1.0	0.4	0.4	0.25	0.1	0.25	0.15

Table 1. Typical chemical compositions of aluminium alloy 5083 (percentage by mass).

2.2 Welding of 5083 aluminium

2.2.1 Pulsed Gas Metal Arc Welding (P-GMAW)

Arc welding is the most widely used process in the shipbuilding, aerospace, pipeline, pressure vessel, automotive and structural industries. In gas metal arc welding (GMAW), the heat required to fuse the metals is generated by an electric arc established between a consumable electrode wire and the workpiece. The electric arc and the molten weld pool are shielded from atmospheric contamination by an externally supplied shielding gas or gas mixture. GMAW may be used in the semi-automatic mode (SA-GMAW), i.e. the filler wire is fed at a constant speed by a wire feeder, while the welder manipulates the welding torch manually, or in the fully-automatic mode (FA-GMAW), i.e. the filler wire is fed continuously at a constant speed, while the torch is manipulated automatically.

With a pulsed power supply, the metal transfer from the tip of the electrode wire to the workpiece during GMAW is controlled. Pulsed current transfer is a spray-type transfer that occurs in pulses at regularly spaced intervals rather than at random intervals. The current is pulsed between two current levels. The lower level serves as a background current to preheat the electrode (no metal transfer takes place), while the peak current forces the drop from the electrode tip to the weld pool. The size of the droplets is approximately equal to the wire diameter. Drops are transferred at a fixed frequency of approximately 60 to 120 per second. As a result, spray transfer can take place at lower average current levels than would normally be the case. Due to the lower average heat input, thinner plates can be welded, distortion is minimized and spatter is greatly reduced. The pulsed GMAW process is often preferred for welding aluminium. The lower average heat input reduces the grain size of the weld and adjacent material and reduces the width of the heat-affected zone (HAZ) [1-3].

The weld penetration, bead geometry, deposition rate and overall quality of the weld are also affected to a large extent by the welding current, arc voltage (as determined by the arc length), travel speed, electrode extension, electrode orientation (or gun angle) and the electrode diameter. Excessive arc voltages or high arc lengths promote porosity, undercut and spatter, whereas low voltages favour narrow weld beads with higher crowns. The travel speed affects the weld geometry, with lower travel speeds favouring increased penetration and deposition rates. Excessively high travel speeds reduce penetration and deposition rate, and may promote the occurrence of undercut at the weld toes [4].

The welding current, arc voltage and travel speed determine the heat input (HI) during welding. This relationship is shown in equation (1);

$$\mathrm{HI} = \eta \frac{VI}{v} \qquad \ldots(1)$$

where: V is the arc voltage (V), I is the welding current (A), v is the travel speed, and η is the arc efficiency factor (typically in the region of 0.7 to 0.8 for GMAW).

The mechanical properties of the welded joint, the weld geometry, occurrence of flaws and level of residual stress after welding depend mainly on the joining process, welding consumable and procedure employed.

2.2.2 Structure of the welds

The filler metal and the melted-back base metal form an admixture. The properties of the weld, such as strength, ductility, resistance to cracking and corrosion resistance, are strongly affected by the level of dilution. The dilution, in turn, depends on the joint design, welding

process and parameters used. A more open joint preparation (for example a larger weld flank angle, ϕ , in Figure 1(a)) during welding increases the amount of filler metal used, reducing the effect of dilution. Joint preparations such as single or double V-grooves are often preferred to square edge joint preparations when welding crack susceptible material with non-matching filler metal [5].

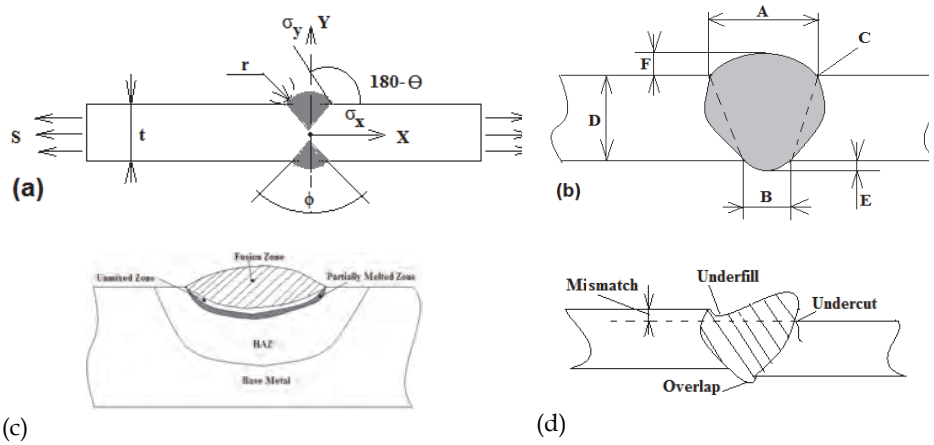

(c)

(d)

Fig. 1. Schematic illustration of (a) geometrical parameters of a typical butt weld with a double V edge preparation, where r is weld toe radius, ϕ weld flank angle and t plate thickness; (b) geometrical structure of a weld, where A is weld face, B the root of the weld, C weld toe, D the plate thickness or weld penetration, E root reinforcement, and F face reinforcement; (C) compositional structure of a typical weld; and (d) geometric weld discontinuities.

The thermal cycle experienced by the metal during welding results in various zones that display different microstructures and chemical compositions (Figure 1(c)). The fusion zone (composite zone or weld metal) melts during welding and experiences complete mixing to produce a weld with a composition intermediate between that of the melted-back base metal and the deposited filler metal. The unmixed zone cools too fast to allow mixing of the filler metal and molten base metal during welding, and displays a composition almost identical to that of the base metal. The partially melted zone experiences peak temperatures that fall between the liquidus and solidus temperatures of the base metal. HAZ represents the base metal heated to high enough temperatures to induce solid-state metallurgical transformations, without any melting [4].

Most welds contain discontinuities or flaws that may be design or weld related, with the latter category including defects such as undercut, slag or oxide inclusions, porosity, overlap, shrinkage voids, lack of fusion, lack of penetration, craters, spatter, arc strikes and underfill. Metallurgical imperfections such as cracks, fissures, chemical segregation and lamellar tearing may also be present. Geometrical discontinuities, mostly associated with imperfect shape or unacceptable bead contour, are often associated with the welding procedure and include features such as undercut, underfill, overlap, excessive reinforcement and mismatch (Figure 1(d)) [4].

Aluminium welds are also very susceptible to hydrogen-induced porosity. The weld pool may dissolve large amount of hydrogen from the arc atmosphere. On solidification, the solubility of hydrogen decreases and the entrapped hydrogen forms gas porosity. Typical sources of hydrogen contamination are lubricant residues, moisture and the hydrated surface oxide on the base metal or filler wire surface. These defects act as stress concentrations and may lead to rapid fatigue crack initiation if the weld is exposed to fluctuating stresses of sufficient magnitude [5-6].
Most weld flaws can be removed by grinding, machining and/or flush polishing, thereby improving the mechanical properties, corrosion resistance and fatigue properties of the joint. Subsurface flaws, which are more prevalent during SA-GMAW than FA-GMAW, are more difficult to detect and correct.

2.2.3 Weldability of aluminium 5083

Pure aluminium exhibits high electrical conductivity, about 62% of that of pure copper. Very little resistance heating occurs during welding, and high heat inputs are therefore necessitated when joining aluminium and its alloys to ensure complete fusion. Incomplete fusion may also result from the presence of a hydrated aluminium oxide layer that forms spontaneously on exposure to air or water due to the strong chemical affinity of aluminium for oxygen. This layer melts at about 2050°C, significantly above the melting range of aluminium. In order to prevent poor fusion, the aluminium oxide layer needs to be removed prior to or during welding. Suitable fluxes, chemical or mechanical cleaning methods, or the cleaning action of the welding arc in an inert atmosphere (cathodic cleaning) can be used to remove the oxide [4]. The high thermal expansion coefficient of aluminium (about twice that of steel) may result in distortion and high levels of residual stress in the welds, and precautions need to be taken to control distortion to within acceptable limits.
The weldability of aluminium, defined as the resistance of the material to the formation of cracks during welding, is affected by the physical properties (Table 2), chemical composition and prior temper state of the material [4-5]. As long as dilution is controlled to a minimum, these alloys can, however, be welded successfully using non-matching filler metal.

Base Metal	*Chemical Composition, wt %*						*Melting point, °C*	*TC at 25°C, W/m.K*	*EC, % IACS*	*GMAW W*
	Al	*Mg*	*Si*	*Mn*	*Cr*	*Cu*				
5083	Bal.	4.4	-	0.7	0.15	-	574-638	117	29	A

Where TC the thermal conductivity, EC the electrical conductivity, W the weldability and A indicates that the alloy is readily weldable.

Table 2. Typical chemical composition, physical properties and weldability of wrought aluminium alloy 5083 [4].

A dissimilar filler metal with a lower solidus temperature than the base metal is generally employed so that the hardenable base metal is allowed to completely solidify and develop some strength along the fusion line before weld solidification stresses develop. Filler wires containing approximately 5% silicon, such as ER4043, may be used. ER4043 filler wire solidifies and melts at temperatures lower than the solidification temperature of the base metal. Contraction stresses, which could cause cracking, are relieved by the plasticity of the still liquid filler metal, preventing the formation of cracks. The Al-Mg and Al-Mg-Mn filler alloys, such as ER5356 and ER5183, are employed more frequently as welding consumables

since these materials provide an optimum combination of mechanical properties, corrosion resistance and crack resistance. The chemical compositions of these filler wires are shown in Table 3.
Aluminium alloys 5083 are normally welded with near-matching filler metal. Consumables, such as ER5356 and ER5183, increase the strength of the weld and reduce the crack sensitivity [5].

Filler Metal	*Chemical Composition, wt %*						*Melting range, °C*
	Al	*Mg*	*Si*	*Mn*	*Cr*	*Ti*	
ER4043	Bal.	-	5.25	-	-	-	574-632
ER5183	Bal.	4.75	-	0.75	0.15	-	579-638
ER5356	Bal.	0.12	-	0.12	0.12	0.13	571-635

Table 3. Chemical composition and melting point of filler metals typically used in joining aluminium alloys [4].

The mechanical properties, fatigue performance and corrosion resistance of the welded joint depend on the filler metal used, and an optimal filler wire for a specific application needs to be selected [5]. Tables 4 and 5 provide guidance on the selection of filler metals for welding 5083 aluminium.

Strength	*Ductility*	*Colour match*	*NaCl corrosion resistance*	*Least cracking tendency*
ER5183	ER5356	ER5183	ER5183	ER5356
	ER5556	ER5356		ER5183

Table 4. Recommended filler metals for welding 5083 [5].

Filler Alloys	*Filler Characteristics*				
	Ease of welding	*As welded strength*	*Ductility*	*Corrosion resistance*	*Colour match*
ER5183	A	A	B	A	A
ER5356	A	-	A	A	A

where: A, B, C and D are relative ratings, with A: best and D: worst.

Table 5. Filler metal selection for 5083 welds [4].

As shown in Tables 4 and 5, filler metal selection plays a major role in determining the corrosion resistance of the welded joint. The corrosion resistance is also affected by the cleanliness of the alloys, the chemical and physical environment and the welding process. In the as-welded condition, however, the weld metal and HAZ, and any welding defects, are most likely to become preferential corrosion sites.

2.3 Corrosion resistance of 5083 aluminium alloy

Aluminium and its alloys generally exhibit good corrosion resistance in a wide range of environments. The corrosion resistance of aluminium is derived from a thin, hard and compact film of adherent aluminium oxide that forms spontaneously on the surface. This thin oxide film, only about 5 nm (or 50 Å) in thickness, grows rapidly whenever a fresh

aluminium surface is exposed to air or water. Aluminium oxide is dissolved in some chemical solutions, such as strong acids and alkalis, leading to rapid corrosion. The oxide film is usually stable over a range of pH values between 4.0 and 9.0, with water soluble species forming at low pH (Al^{3+}) and high pH (AlO_2^-) values (see Pourbaix diagram, Figure 2(a)) [7-8].

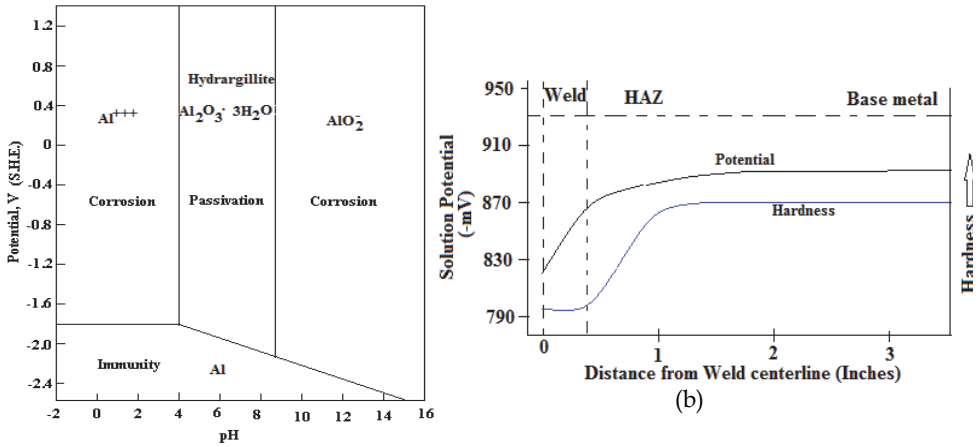

Fig. 2. (a) Pourbaix diagram for aluminium with areas representing the hydrated oxide film of hydrargillite($Al_2O_3.3H_2O$), and the dissolved species Al^{3+} and AlO_2^- at 25°C (potential values are given relative to the standard hydrogen electrode). (b) Schematic illustration of the change in solution potential and hardness in the weld metal and HAZ of 5083.

The corrosion resistance of 5083 aluminium is normally reduced by welding. An area within about 25 mm on either side of the weld tends to exhibit lower corrosion resistance [4].

2.3.1 Corrosion of 5083 welds

The passive oxide films, spontaneously formed on aluminium alloy surfaces, are however, susceptible to localised breakdown at the exposed surface or at discontinuities, which result in high dissolution rates of the underlying metal (pitting corrosion). The chemical composition of the weld metal and HAZ and the presence of inclusions, precipitates and second phases in the welded joint, however, produce slightly different electrode potentials in the presence of an electrolyte (Figure 2(b)). Selective or localized corrosion is therefore possible when the base metal and the weld metal or second phases possess significantly different electrode potentials. A galvanic effect can be created, with the more active region corroding preferentially to protect the more noble region with which it is in contact [4-5,8].
Welds produced by the GMAW process appear to be less resistant to pitting corrosion in salt water solutions than solid state friction stir welds, as reported by Moggiolino and Schmid [9]. Preferential attack occurs in the narrow interface between the weld bead and the HAZ, or between the HAZ and the base metal. As a result of the high peak temperatures experienced by the high temperature HAZ adjacent to the fusion line, grain coarsening, recrystallization and partial dissolution of intermetallic strengthening precipitates occurring during welding.

2.3.2 Mechanism of pitting corrosion in 5083 alloy

Pitting corrosion is a form of localized corrosion that occurs in environments in which a passive surface oxide film is stable. Pits initiate due to local rupture of the passive film or the presence of pre-existing defects, and then propagate in a self-sustaining manner. Localized corrosion can initiate as a result of the difference in corrosion potential within a localized galvanic cell at the alloy surface. These micro-galvanic cells can form at phase boundaries, inclusion/matrix interface regions, and at insoluble intermetallic compounds within the matrix.

The aluminium oxide passive film consists of two superimposed layers with a combined thickness between approximately 4 and 10 nm. The first compact and amorphous layer, in contact with the alloy, forms as soon as the material comes into contact with air or water, within a few milliseconds, according to the reaction shown in equation (2):

$$2Al + 3/2\ O_2 \rightarrow Al_2O_3 \quad (\Delta G = -1675\ kJ) \qquad \ldots(2)$$

The second layer grows over the initial film due to a reaction with the corrosive environment, likely by hydration (reaction with water or moisture). The second layer is less compact and more porous, and may react with the corrosive environment (Figure 3(a)) [8].

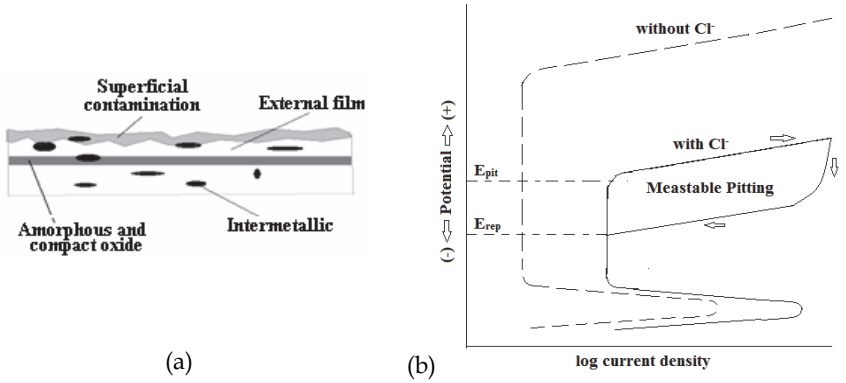

Fig. 3. Schematic illustration of (a) typical structure of the aluminium oxide passive layer; and (b) polarization diagram, illustrating the position of the critical pitting potential, E_{pit}, and the repassivation potential (or protection potential), E_{rep}.

As shown in Figure 3(b), localized breakdown of the passive film initiates above the critical pitting potential (E_{pit}). The pitting potential is often stated to quantify the resistance of a material to pitting corrosion, and represents the potential in a particular solution above which stable pits may form. More noble pitting potential values (E_{pit}) signify increased resistant to pitting corrosion. The presence of aggressive anionic species, such as chloride ions (which increase the potentiostatic anodic current at all potentials) increase the likelihood of pitting corrosion.

The value of E_{pit} in NaCl solution remains unaffected by the dissolved oxygen concentration and moderate temperature variations (0°C to 30°C). At temperatures above 30°C, the pitting corrosion rate increases considerably. A rough surface finish increases susceptibility to pitting corrosion and reduces the pitting potential. The repassivation or protection potential (Figure 3(b)) represents the minimum potential at which existing pits can propagate, but new pits cannot form.

As described above, pitting corrosion typically develops in the presence of chloride ions (Cl^-). The chloride ions are adsorbed on the aluminium oxide layer, followed by rupture of the oxide film at weak points, with formation of micro-cracks that are a few nanometres wide. At the same time, oxygen is reduced on cathodic sites and rapidly oxidizes aluminium by forming an intermediate complex chloride, $AlCl^{4-}$, in areas associated with cracks in the oxide film [7-8].
As the pit deepens, the rate of transport of ions out of the pit decreases. The pit current density therefore tends to decrease with time, owing to an increase in the pit depth and ohmic potential drop. Repassivation may also occur if dissolution rate of the bottom of the pit is insufficient to replenish the loss of aggressive environment due to reaction, and the pit may stop growing after few days. Pitting can continue on fresh sites. Al^{3+} ions, highly concentrated in the bottom of the pit, diffuse towards the pit opening and react with the more alkaline solution on the plate surface, facilitating the formation of $Al(OH)_3$. Hydrogen micro-bubbles formed in the pit may transport the $Al(OH)_3$ to the pit opening where it forms an insoluble deposit that appears as white eruptions around the pit surface. The formation of positively charged Al^{3+} ions in the bottom of the pit may also attract Cl^- ions towards the underside of the pit, encouraging the formation of $AlCl^{4-}$ (through the reaction $Al^{3+}+Cl^-+6e^-\rightarrow AlCl^{4-}$), as shown in Figure 4. The accumulation of $Al(OH)_3$ forms a dome at the pit surface which progressively blocks the pit opening. This can hinder the exchange of Cl^- ions which may progressively retard or even arrest pit growth. A corrosion pit may therefore be considered as a local anode surrounded by a matrix cathode. Once pitting corrosion has initiated, pit growth becomes sustainable at lower potentials than the pitting potential [7-8,10].

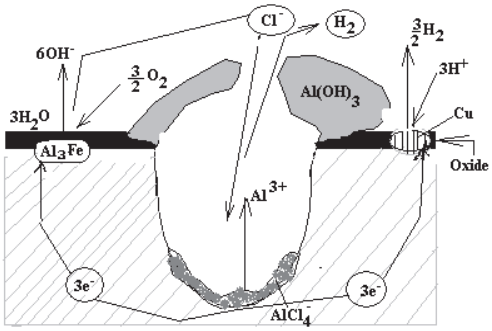

Fig. 4. Schematic illustration of the mechanism of pitting corrosion in aluminium.

Cold working generally reduces the corrosion resistance of the magnesium-alloyed grades, as the β-Al_3Mg_2 phase may precipitate on grain boundaries and dislocations, increasing susceptibility to stress corrosion cracking. Inclusions, impurities, pores, vacancies, dislocation walls and grain boundaries may generate galvanic cells in 5083 alloy. Cored structures promote galvanic interaction and point defects are usually more anodic than the surroundings [8,10].
Intermetallic phases, such as Al_3Mg_2, Al_3Mg_5 and Mg_2Si, are anodic with respect to the 5083 alloy matrix (Table 6), and promote rapid localized attack through galvanic interaction. Less electronegative intermetallic phases, such as Al_3Fe and Al_6Mn, are cathodic with respect to the 5083 aluminium matrix, leading to preferential dissolution of the alloy matrix [8,11-12].

Metal, alloy or intermetallic phase	*Potential, (V)*
Al_8Mg_5	-1.24
Mg_2Si (intermetallic phase)	-1.19
Al_3Mg_2 (intermetallic phase)	-1.15
Mg	-0.85
Al_6Mn (intermetallic phase)	-0.80
Al5083, Al5183	-0.78
Al_3Fe (intermetallic phase)	-0.51

Table 6. Relative electrochemical potentials for aluminium alloys and typical intermetallic phase in a NaCl solution (Potential versus standard calomel electrode) [8-13].

The pit density (spacing), the pit size and pit depth can be used to evaluate the pitting corrosion resistance of alloys. A pit depth measurement using an optical microscope is often the preferred way of evaluating pitting corrosion. The pitting factor (*p/d)* may also be used, where *p* is the maximum pit depth and *d* is the average pit depth. The pit depth increases, not only with time, but also with surface area, and can be estimated using equation (11):

$$d_1=Kt_1^{1/3} \quad \ldots(3)$$

where: d_1 is the pit depth at time t_1 and k is a constant.
The presence of a weld often promotes corrosion due to changes in the local microstructure and precipitate distribution, and the increased likelihood of defects. Welding also affects the mechanical properties of the aluminium alloy in the vicinity of the joint. Any localized change in mechanical properties can, in turn, influence the corrosion behaviour and the fatigue properties of the material.

2.4 Mechanical properties of welded 5083 aluminium

Aluminium alloys 5083, produced via ingot casting, and cold working, contain precipitates that interact with moving dislocations, thus increasing strength at room temperature. When these alloys are welded, however, the precipitates dissolve and/or coarsen, reducing the mechanical strength significantly. This reduction in mechanical properties can be attributed to annealing and recrystallization, grain growth and precipitate dissolution and/or overageing; and uncontrolled grain boundary precipitation on cooling [14].
The HAZ of 5083 aluminium alloy is completely annealed and recrystallized during welding. The effect of any prior work hardening is lost when such an alloy is exposed to a temperature above 343^{o}C for only few seconds. A reduction in hardness is therefore observed in the HAZ [14]. The degree of softening is mainly affected by the heat input, the welding technique, the size of the workpiece and the rate of cooling. Low heat input levels reduce the time at temperature and increase the cooling rate, thereby minimizing the degree of softening in the HAZ. Pulsed GMAW has the advantage of ensuring good penetration and adequate fusion at lower average heat input levels [4]. The amount of grain growth is reduced and the width of the HAZ minimized.
Welds in 5083 alloy display reasonable ductility and high strength when near-matching filler metals are used (Table 7).

Base Alloy	*Filler Metal*	*Ultimate Tensile Strength, MPa*	*Minimum. Yield Stress, MPa*	*Tensile Elongation, % (50.8mm gauge)*	*Free Bending Elongation, %*
5083	5183	276-296	165	16	34
5083	5356	262-241	117	17	38

Table 7. Mechanical properties of butt joints in aluminium 5083 welded using ER5183 and ER 5356 filler metals [4].

2.5 Fatigue behaviour of welds

Fatigue is a highly localised and permanent structural change involving the initiation and propagation of a crack under the influence of fluctuating stresses at levels well below the static yield stress required to produce plastic deformation. Under these conditions, fatigue cracks can initiate near or at discontinuities lying on or just below the free surface. These discontinuities may be present as a result of mechanical forming, or welding and cause stress concentrations in the form of inclusions, second phases, porosity, lack of fusion, lack of penetration, weld toe geometry, shape changes in cross section, corrosion pits and grain boundaries [4]. The fluctuating applied stress (amplitude stress (S_a)) leads to plastic deformation (long-range dislocation motion) which produces slip steps on the surface. The dislocations may concentrate around obstacles, such as inclusions or grains boundaries, promoting fracture of inclusions or second phase particles, decohesion between the particles and the matrix, or decohesion along grain boundaries. The lowest fatigue strength is usually associated with the highest stress concentration at the metal surface. The weld toe represents a sharp stress concentration in transversely loaded welds (Figure 5) and fatigue cracks often initiate at the weld toe, followed by propagation into the base metal. Uneven root profiles can cause crack initiation at the weld root, followed by propagation into the weld metal. Stop/start positions and weld ripples can act as stress concentrations in longitudinal welds. Lack of penetration and undercut are severe stress raisers and can accelerate fatigue crack initiation, whereas internal defects (such as porosity and slag inclusions) usually only initiate fatigue cracks if surface stress concentrations are removed. Geoffroy *et al*. [6] confirmed that poor weld quality causes a significant reduction in fatigue life.

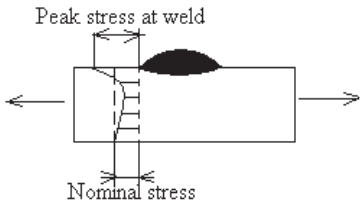

Fig. 5. Stress concentration caused by the weld toe geometry.

The formation of residual stresses in welds is a consequence of the expansion and contraction of the weld metal and base metal close to the heat source and the restraining effect of the adjacent base alloy at lower temperatures. On cooling, high tensile residual stresses in the weld metal and HAZ are balanced by compressive residual stresses in the adjacent plate material. The presence of high tensile residual stresses in the weld metal and HAZ has two important consequences. First, fatigue failure can occur under loading

conditions that, nominally, introduce compressive stresses, and second, the fatigue strength of welded joints is often governed by the applied stress range regardless of the nominal applied stress ratio. Due to the lower tensile strength of welds in aluminium alloys, the applied stress ratio may influence the fatigue strength of the joint to a limited extent, but fatigue design is usually based on the stress range and a single *S-N* curve represents the performance of a given welded joint for any minimum/maximum ratio of load input [15].

2.6 Corrosion fatigue performance of 5083 aluminium

The fatigue behaviour of magnesium-alloyed aluminium after welding is determined by the weld microstructure and mechanical properties. Any stress concentration caused by a second phase particle of identifiable size and shape can nucleate a crack in a non-corrosive environment. This effect is enhanced in a corrosive environment where corrosion pits are often associated with second phase particles in the matrix. Such a combination of a pit and a second phase particle may present a greater stress concentration than a pit or particle alone. Precipitates, second-phase particles, pores and grain boundaries within the matrix facilitate the nucleation and growth of corrosion pits in aggressive media and promote fatigue crack initiation and growth.

Under corrosion fatigue conditions, the shape of the fatigue loading cycle, the frequency and any periods of rest have a considerable influence on the fatigue life. The growth rate of corrosion pits increases with increasing stress amplitude and cyclic stress frequency [6]. The corrosion fatigue fracture surface may be characterised as describe below.

2.6.1 Features of corrosion fatigue fracture surfaces

The characterization and understanding of the kinetics and mechanisms of corrosion fatigue are indispensable to the service life prediction, fracture control and development of fatigue resistant alloys. Corrosion fatigue is characterized as brittle failure caused by the combined effect of a fluctuating stress and a corrosive environment. The principal feature of this fracture mode is the presence of corrosion products and beach marks on the fracture surface [16].

In corrosion fatigue cracking (CFC), anodic dissolution at the root of the crack is facilitated by repeated rupture of the passive film at the crack tip by fatigue processes and the subsequent repassivation of the newly exposed metal surface. The mechanism of anodic dissolution may involve rupture of the brittle oxide layer, selective dissolution or dealloying, and/or corrosion tunnelling. The growth rate of a crack during environmentally-assisted corrosion fatigue is therefore controlled by the rate of anodic dissolution, the rupture of the oxide film, the rate of repassivation, the mass transport rate of the reactant to the dissolving surface and the flux of dissolved metal cations away from the surface. Anodic dissolution (commonly referred to as active path dissolution, slip dissolution, stress/strain enhanced dissolution or surface film rupture/metal dissolution) is the CFC mechanism by which the crack growth rate is enhanced by anodic dissolution along susceptible paths that are anodic to the surrounding matrix. Such susceptible paths can include grain boundaries, strained metal at the crack tip and the interface between second-phase particles and the matrix.

In this mechanism, a slip step is formed at the crack tip under fatigue loading conditions and fractures the protective surface oxide film. The freshly exposed metal surface at the crack tip reacts with the aggressive solution and partly dissolves until the crack tip repassivates and the oxide layer is restored. This process repeats during successive fatigue

loading cycles as slip-steps break the oxide layer and fresh material is exposed to the corrosive environment. Factors affecting this process are mechanical variables (frequency, stress and waveform of the loading cycle), geometrical variables (crack size, weld geometry and specimen thickness), metallurgical variables (alloy chemical composition, microstructure, and the strength and toughness of the material), and environmental variables (electrolyte, corrosion species concentration and temperature) [8].
One of the most important parameters affecting the susceptibility to CFC is the loading frequency. The lower the frequency of the applied loading cycle, the higher the crack propagation rate per cycle (da/dN). Very high frequencies can completely eliminate the effect of the corrosive environment on fatigue by minimizing the interaction time between the environment and the crack tip [17].
As described earlier, the presence of corrosion pits induces stress concentrations responsible for promoting crack initiation. As the pit depth increases, the stress levels in the surrounding material increase. When the stress level reaches a threshold value (determined by the alloy microstructure and the corrosive environment), a crack is initiated. As reported by Pidaparti *et al*. [17], closely spaced pits and longer exposure times increase the stress levels in the material surrounding the corrosion pits, promoting crack initiation.
The influence of corrosion pits on fatigue crack initiation has been reported by a number of authors for various aluminium alloys. Chlistovsky *et al*. [18] showed that the fatigue life of 7075-T651 alloy is significantly reduced in 3.5% NaCl corrosive environment. This reduction is attributed to the initiation of cracks from stress concentrations caused by pit formation, and a combination of anodic dissolution at the crack tip and hydrogen embrittlement. A similar observation was made by Chen *et al*. [19] who studied the corrosion fatigue behaviour of aluminium 2024-T3. Their fractographic study revealed that fatigue cracks nucleated from one or two of the larger pits observed on the surface.
In order to study the corrosion fatigue behaviour of 5083 alloy in air and corrosive environment, fatigue testing has to be performed.

2.6.2 Corrosion fatigue testing

Laboratory fatigue testing can be categorized as crack initiation (fatigue life) testing or crack propagation testing. The loading mode can be direct or axial, plane bending, rotating beam, alternating torsion or a combination of these modes.
It is necessary for general design purposes to have fatigue data for positive and negative values of maximum stress (S_{max}), minimum stress (S_{min}) and S_m to cater for varying stress conditions. In this respect, a characterizing parameter known as the stress ratio, R, (given by, $R = S_{min} / S_{max}$) is often used in presenting fatigue data.
Fatigue test data is typically presented in the form of a S_a-log N_f curve, known as Wöhler's curve. Basquin [20] showed that a typical S_a-log N_f plot can be linearized with full log coordinates, thereby establishing the exponential law of fatigue shown in equation (4).

$$N (S_a)^p = C \tag{4}$$

where: N is the number of cycles, S_a is the stress amplitude, and C and p are empirical constants.
To perform corrosion fatigue testing, an environmental chamber of glass or plastic containing the electrolyte is introduced during testing. To minimize galvanic effects, the specimen must be gripped outside of the test solution. The solution is circulated through the

corrosion chamber, which is sealed to the specimen. In this testing method, factors that influence the number of cycle to failure include the stress amplitude (S_a), the stress ratio (R), chemical concentration of dissolved species such H^+, O^{2-}, and other ions, the alloy properties (such as yield stress, hardness and microstructure), the waveform of the loading cycle, the test temperature and the electrolyte flow rate [17].

3. Research methodology

In order to evaluate the fatigue properties of aluminium 5083-H111 welds in the ambient atmosphere and in a 3.5% NaCl solution, the experimental procedure described below was followed during the course of this investigation.

3.1 Welding procedure

Flat aluminium sheets (with initial dimensions of 2000 mm long, 120 mm wide and 6.35mm thick) of aluminium alloy 5083-H111 (with chemical compositions given in Table 8) were supplied for examination. The -H111 temper designation in the case of the non-hardenable 5083 alloy refers to material strain-hardened to a level below that required for a controlled -H11 temper (corresponding to one eighth of the full-hard condition). These samples were joined using, pulsed SA-GMAW or FA-GMAW, as shown in Figure 6. Prior to welding, the plates for SA-GMAW were prepared with a double-V edge preparation, degreased with acetone and preheated to approximately 100ºC. The FA-GMAW welds were performed with a square edge preparation. Three different aluminium filler wires were used, namely ER4043 (Al-Si), ER5183 (Al-Mg) and ER5356 (Al-Mg) (with typical chemical compositions given in Table 9).

Element %	*Al*	*Mg*	*Mn*	*Fe*	*Si*	*Cr*	*Cu*	*Zn*	*Ti*	*Others total*
5083-H111	Balance	3.66	0.39	0.40	0.22	0.14	0.04	0.03	0.02	<0.001

Table 8. Chemical compositions of the 5083-H111 aluminium plate material (percentage by mass).

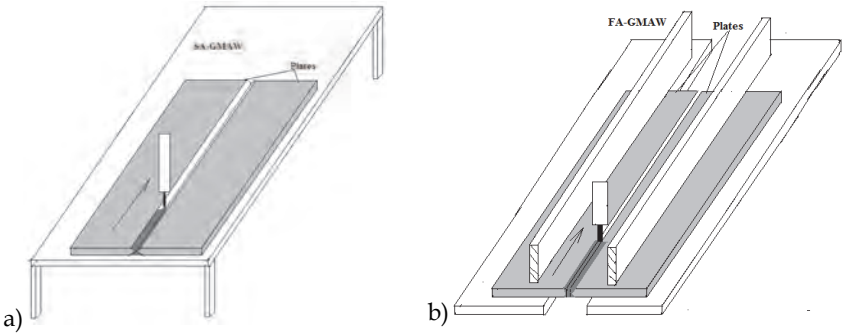

Fig. 6. Schematic illustration of the pulsed GMAW process: (a) SA- GMAW; and (b) FA-GMAW.

Element %	*Al*	*Mg*	*Mn*	*Fe*	*Si*	*Cr*	*Cu*	*Zn*	*Ti*	*Others total*
ER4043	Balance	0.05	0.05	0.80	4.5-6.0	Not specified	0.30	0.10	0.20	Be 0.0008%
ER5183	Balance	4.3-5.2	0.50-1.0	0.40	0.40	0.05-0.25	0.10	0.25	0.15	Not specified
ER5356	Balance	4.5-5.5	0.05-0.2	0.40	0.25	0.05-0.20	0.10	0.10	0.06-0.20	Be 0.0008%

Table 9. Typical chemical compositions of filler wires (percentage by mass, single values represent minimum levels).

5083-H111 aluminium plates were welded in horizontal position using argon shielding gas. The welding parameters were selected to ensure a spray transfer mode for all the welds, and are given in Table 10.

Parameters	*Arc voltage*	*Welding current*	*Wire feed rate*	*Wire diameter*	*Nozzle to plate distance*	*Travel speed*	*Torch angle*	*Gas flow rate*
Unit	*V*	*A*	*m/min*	*mm*	*mm*	*m/min*	*Degrees*	*l/min*
SA-GMAW	24-29	133-148	6.1-7.6	1.2-1.6	15-20	0.8-1	60-80	18-33
FA-GMAW	20-23	133-148	6.1-7.6	1.2-1.6	15-20	0.4-0.6	60-80	19-28

Table 10. Measured pulsed gas metal arc welding process parameters.

3.2 Material characterization

In order to analyse the aluminium samples and to quantify the material properties that may influence fatigue resistance, the microstructures of the as-machined and as-welded specimens were analysed, the hardness was measured and tensile tests were performed. The corrosion resistance in 3.5% NaCl solution was evaluated using immersion testing.

3.2.1 Microstructural analysis

As-supplied and as-welded samples were sectioned and machined to produce rectangular fatigue and tensile specimens, with dimensions shown schematically in Figure 7. Samples were removed for microstructural examination in the long transverse (LT) direction, longitudinal (LD) direction and short transverse (ST) direction (Figure 7). Samples were prepared for microstructural analysis and etched using Keller's reagent as described in ASTM standard E340 [17]. The metallographic samples were examined with an inverted optical microscope (with Image-Pro PLUS 5.1™ or IMAGEJ™ image analysis software), and a scanning electron microscope (SEM) equipped with Energy Dispersive X-ray Spectroscopy (EDS) capabilities. The grain sizes were determined using the line intercept method.

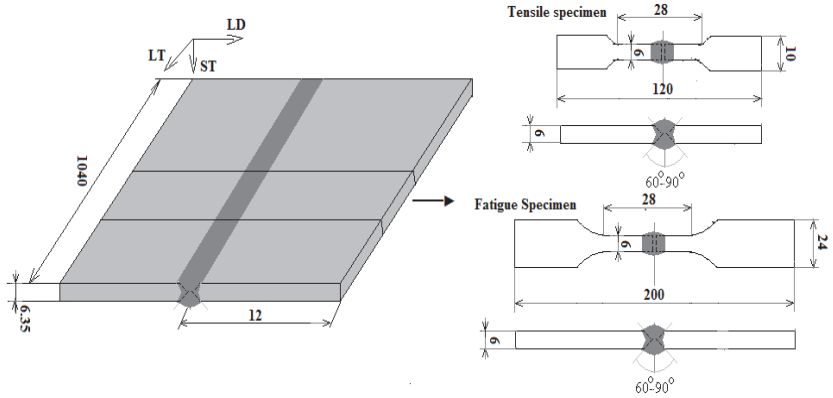

Fig. 7. Dimensions of the tensile and fatigue specimens machined from the welded plates.

3.2.2 Hardness measurements

In order to perform hardness measurements, machined specimens, in the as-supplied and welded condition, were wet-ground and polished using 1 µm diamond suspension, followed by final polishing using 50 nm colloidal silica, as described in ASTM standard E3 [21]. As-welded specimens were ground flush and polished to allow hardness measurements on the LT-LD plane (Figure 7).

Vickers hardness and Vickers micro-hardness tests were then performed according to the requirements of ASTM standards E92 and E384 [22]. An applied load of 100 grams and a holding time of 10 seconds were employed for the micro-hardness measurements. A hardness profile from the centreline of the weld, through HAZ, to the unaffected base metal was measured at 0.05 to 0.1 mm intervals.

3.2.3 Tensile testing

Tensile tests were performed according to ASTM standard E8-04 [13, 23], on unwelded, as-welded and dressed welded specimens. The machined specimens (Figure 7) were wet-ground flush in the longitudinal direction (LD) to remove all machining marks for unwelded and weld reinforcing for dressed weld specimens. Undressed welded specimens were wet-ground without changing the weld toe geometry. An INSTRON™ testing machine equipped with *FASTTRACK2*™ software was used to axially stress specimens at a cross head speed of 3.0 mm/min. The 0.2% offset proof stress, ultimate tensile strength and percentage elongation of unwelded and welded specimens were collected for comparison and evaluation.

3.2.4 Corrosion testing

Machined specimens for corrosion testing, in the as-supplied and as-welded condition, were wet-ground and polished. These specimens were cleaned and dried to remove dirt, oil and other residues from the surfaces. Immersion tests were then performed in NaCl solution using a Plexiglas corrosion cell (Figure 8) with a volume of 25 litres of salt water (3.5% NaCl by weight), according to the requirements of ASTM standards G31 [24] and G46 [25]. The 3.5% NaCl simulated sea water was prepared by dissolving 3.5 ± 0.1 parts by weight of

NaCl in 96.5 parts of distilled water. The pH of the salt solution, when freshly prepared, was within the range 6.9 to 7.2. Dilute hydrochloric acid (HCl) or sodium hydroxide (NaOH) was used to adjust the pH during testing. The ambient test temperature varied from 16°C to 27°C. Fresh solution was prepared weekly.

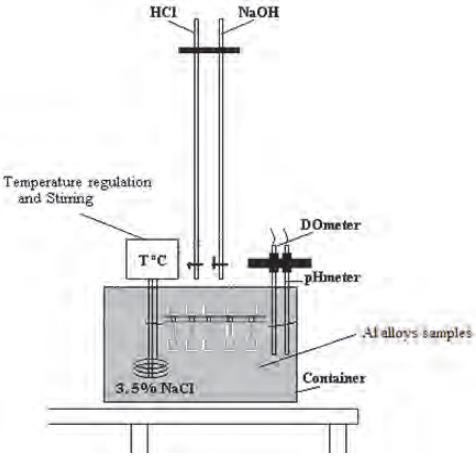

Fig. 8. Schematic illustration of the immersion test in 3.5% NaCl solution.

After a specific time of exposure the specimens were gently rinsed with distilled water and then cleaned immediately to prevent corrosion from the accumulated salt on the specimen surface. Loose products were removed by light brushing in alcohol. The specimens were then immersed in a 50% nitric acid solution for 2 to 4 minutes, followed by immersion in concentrated phosphoric acid for another 5 minutes, to remove bulky corrosion products without dislodging any of the underlying metal. The specimens were then cleaned ultrasonically and dried. The corroded specimens were examined after cleaning, to identify the type of corrosion and to determine the extent of pitting. The samples were inspected visually and microstructurally using Optical Microscope (OM) and SEM. One of the parameters used to quantify the pitting susceptibility was the pit depth, measured using the microscopic method described in ASTM standard G46 [26]. A single pit was located on the sample surface and centred under the objective lens of the microscope at low magnification. The magnification was increased until most of the viewing field was taken up by the pit. The focus was adjusted to bring the lip of the pit into sharp focus and the initial reading was recorded from the fine-focus adjustment. The focus was then readjusted to bring the bottom of the pit into sharp focus and the second reading taken. The difference between the final and the initial readings represents the pit depth. For comparison purposes, photographs and data on the pit sizes and depths were collected for pitting susceptibility evaluation.

3.2.5 Fatigue life assessment

Specimens were fatigue tested in air and in 3.5% NaCl simulated seawater environment using the crack initiation or fatigue life testing method. The specimen was subjected to number of stress cycles (stress controlled, *S-N*) required to initiate and subsequently grow the fatigue crack to failure for various stress amplitudes.

3.2.6 Fatigue testing in air

The axial fatigue life testing method was used to determine the fatigue properties of the specimens, as it takes into account the effect of variations in microstructure, weld geometry, residual stress and the presence of discontinuities.

The machined fatigue specimens (Figure 7) were ground flush and polished in the longitudinal direction to dress some of the welds. This negated the effect of the weld geometry on the fatigue resistance of the dressed welds. Undressed welded specimens were wet-ground in such a way that the weld toe geometry was not changed. The fatigue tests were performed using a symmetric tension-tension cycle (with a stress ratio R = 0.125) to keep the crack open during testing. A constant frequency of 1 Hz was used for all fatigue tests and the number of cycles to failure (N_f) was recorded for each specimen. To ensure repeatability, three to six tests were performed at each stress amplitude, depending on the quality of the weld. The number of cycles recorded to failure was then statistically. The fatigue tests in ambient air were performed at temperatures ranging between 17°C and 21°C and at relative humidity levels between 35.7 and 70.6% RH (relative humidity). INSTRON™ testing machines, equipped with calibrated load transducers, data recording systems and FASTTRACK™ software, were used to fatigue specimens to failure under amplitude stress control, as required by ASTM standard E466-02 [26]. Welded specimens were inspected before testing and any specimens with visual welding defects, such as large pores, underfill or excessive undercut, were discarded. The fatigue specimens were cleaned with ethyl alcohol prior to testing to remove any surface oil, grease and fingerprints. Care was taken to avoid scratching the finished specimen surfaces.

Following testing, the S-N_f curve (represented as stress amplitude-log N_f) was determined from the median number of cycles to failure at each stress level. The fracture surfaces were examined using a low magnification stereo microscope and a scanning electron microscope to reveal the primary crack initiation sites and mode of fracture.

3.2.7 Corrosion fatigue testing in 3.5% NaCl simulated seawater

A corrosion environment consisting of 3.5% NaCl in distilled water was used with the axial fatigue life testing method to investigate the effect of pitting corrosion on fatigue life. The corrosion chamber was designed and manufactured from Plexiglas (Figures 9(b) and 10) in such a way that the specimen was gripped outside the chamber (to prevent galvanic effects) and the chamber was sealed by rectangular rings away from the high-stress gauge section. The NaCl solution was re-circulated from 25 litre storage containers at a constant flow rate by means of a peristaltic pump.

The dissolved oxygen (DO) content, NaCl solution flow rate, pH, temperature, stress amplitude (maximum and minimum stress) and frequency were controlled, as shown in Figures 9(a) and 11. A frequency of 1 Hz was used to increase the interaction time between the specimen and the solution. The measured DO content varied between 7 and 8 ppm (parts per million) and the temperature between 17°C and 21°C during testing. The number of cycles to failure (N_f) was recorded for each stress amplitude (S) at the end of the test.

Following testing, the S-N_f curve was determined from the median number of cycles to failure at each stress level. In order to compare the fatigue resistance in air to that in NaCl, the damage ratio, which is the ratio of the fatigue life in the 3.5% NaCl solution to the fatigue life in air ($N_{f\ NaCl}/N_{f\ Air}$), was calculated and presented as a curve of stress amplitude against $N_{f\ NaCl}/N_{f\ Air}$.

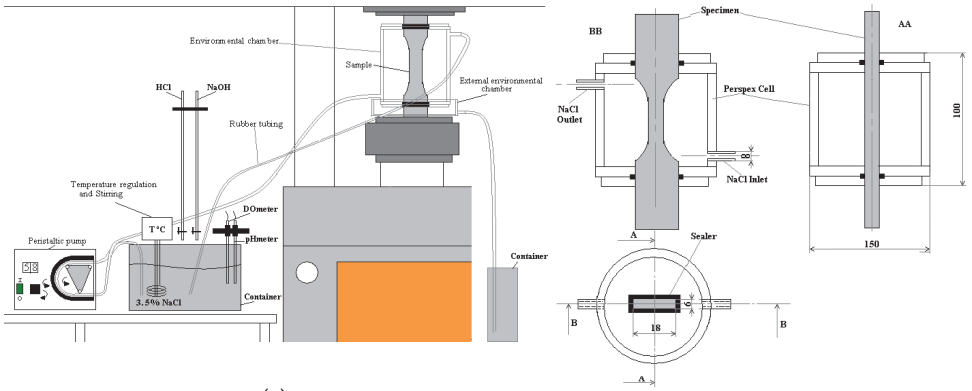

Fig. 9. Schematic illustration of the (a) experimental set-up used for corrosion fatigue testing; (b) corrosion chamber design.

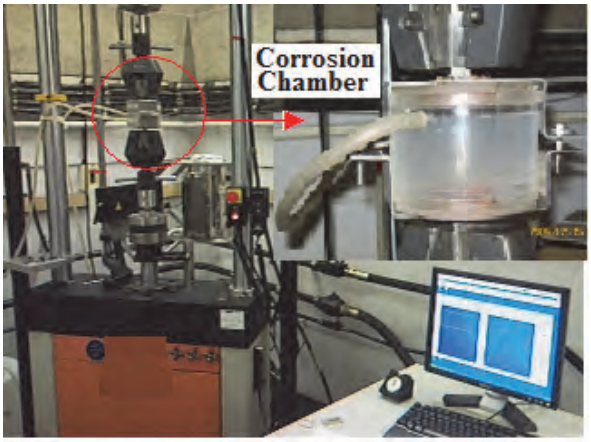

Fig. 10. The experimental set-up used for corrosion fatigue testing in a NaCl solution.

4. Results and discussion

The major findings of this investigation are discussed below.

4.1 Metallographic investigation of 5083-H111 aluminium

The microstructure of the 5083-H111 in the as-supplied condition is shown in Figures 11. Microstructural analysis reveals coarse second-phase particles and fine grain boundary precipitates. The microstructure of plate material appears more equiaxed with an average grain diameter of 24.0 μm (standard deviation of 4.19 μm). Coarse second-phase particles and finer grain boundary precipitates are also evident.

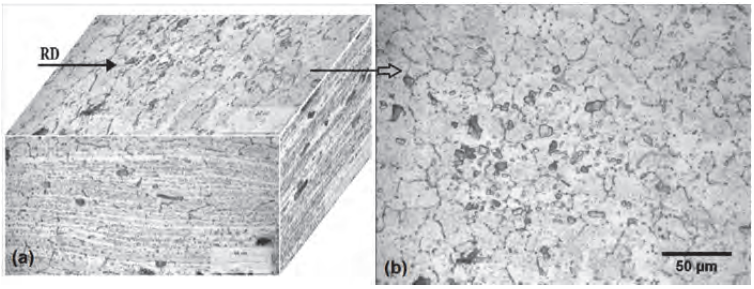

Fig. 11. Microstructures of 5083-H111 aluminium (in the as-supplied condition): (a) in three dimensions, (b) relative to the rolling direction (RD).

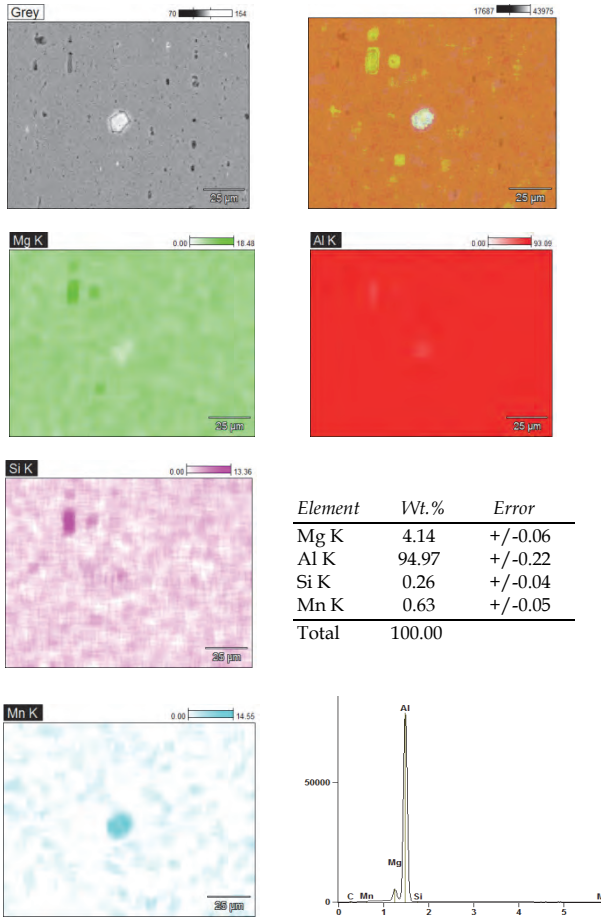

Element	*Wt.%*	*Error*
Mg K	4.14	+/-0.06
Al K	94.97	+/-0.22
Si K	0.26	+/-0.04
Mn K	0.63	+/-0.05
Total	100.00	

Fig. 12. SEM-EDS analysis of second phase particles observed in 5083-H111 in the as-supplied condition.

In order to identify the second phase particles observed in the microstructures, the EDS/SEM and elemental maps were constructed in the vicinity of a number of these particles. Typical elemental maps and EDS analyses of the second-phase particles are shown in Figures 12. The SEM-EDS elemental maps (voltage: 20kv and working distance: 10mm) suggest the presence of two types of particles. A coarse Mg-rich particle (depleted in Mg and Al and slightly enriched in Si) was identified as the Al_6Mn intermetallic phase, whereas smaller particles that appear to be enriched in Mg and Si were identified as an Al-Mg-Si intermetallic phase.
SA-GMAW weld, Figure 13(a), is full penetration joint welded from both sides. Considerable weld reinforcement and some porosity are evident on the macrograph. FA-GMAW welds, Figure 13(b), is full penetration joints welded from one side only, with a smooth profile and some evidence of misalignment and undercut at the weld root. The HAZ (Figure 13(c)) has coarser grain size than the base metal, with coarse second-phase particles, predominantly on grain boundaries. The HAZ grain structures of the SA-GMAW welds appear coarser than those of the FA-GMAW.

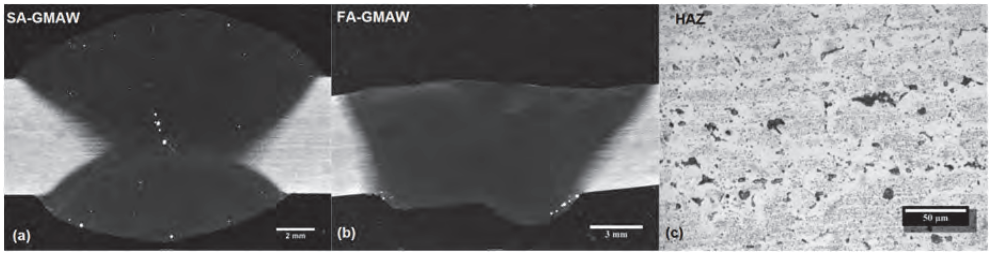

Fig. 13. Representative of 5083-H111 welds: (a) SA-GMAW weld; (b) FA-GMAW weld; and (c) HAZ.

Microstructural examination of the welds (Figure 14(a) to (d)) confirmed the presence of porosity in SA-GMAW welds, and also revealed some lack-of-fusion defects and microcracks in the weld metal. Although all samples with visual welding defects were omitted from mechanical testing, samples with internal flaws and defects were not excluded.

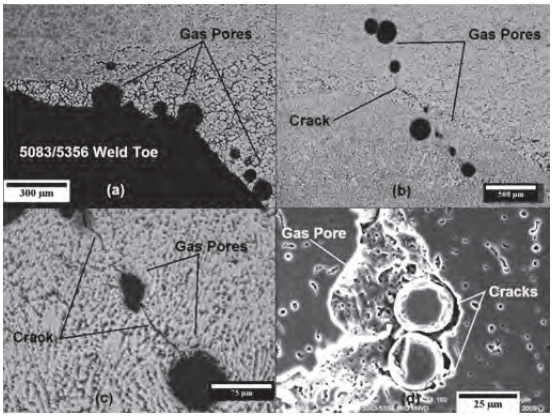

Fig. 14. Defects typically observed in 5083/ER5356 SA-GMAW weld: (a) gas pores, (b)-(d) gas pores and cracks.

Typical optical micrographs of the weld metal welded with ER5356, or ER5183 or ER4043 filler wire are shown in Figures 15(a) to (c). The weld microstructures appear dendritic in structure, characterized by an Al-rich matrix and second phases, present as interdendritic films in the case of ER4043, and as more spherical precipitates in the case of ER5356 and ER5183. Pulsed SA-GMAW welds generally displayed coarser grain structures than FA-GMAW welds.

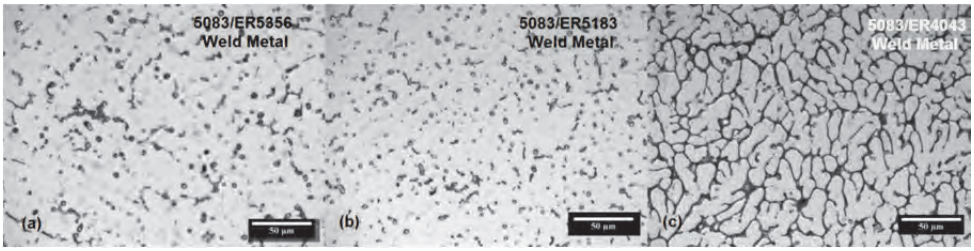

Fig. 15. Typical micrographs of (a) 5083/ER5356; (b) 5083/ER5183; and (c) 5083/ER4043 weld metal.

In order to identify the second phase particles observed in the weld metal, SEM-EDS elemental maps were constructed. A typical elemental map is shown in Figure 16 for a weld performed using ER5356 filler metal. ER5356 welds contain second phase particles and grain boundary regions enriched in Fe and Mg, and slightly depleted in Al. In welds deposited using ER5183 filler wire, second phase particles appear to be enriched mainly in Mg and Al (Figure 17).

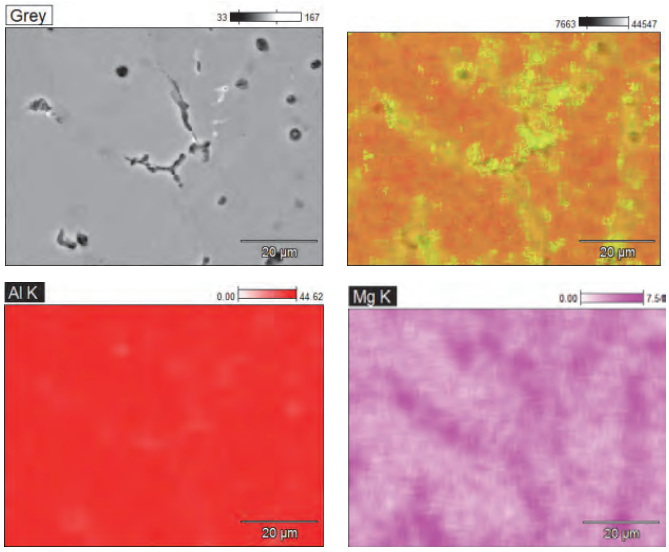

Fig. 16. Part I

Elements	Weight %	%Error
C k	3.46	+/-0.43
O k	1.04	+/-0.11
Mg k	3.82	+/-0.05
Al k	90.66	+/-0.20
Si k	0.22	+/-0.04
Fe k	0.22	+/-0.04
Mn k	0.57	+/-0.04
Total	100.00	

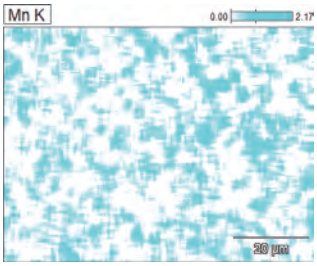

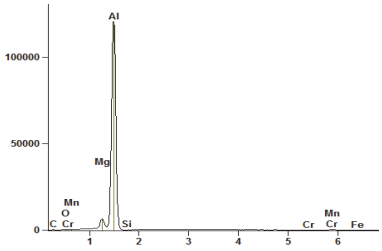

Part II

Fig. 16. Typical EM-EDS analysis of second phase particles observed in a weld performed using ER5356 filler wire.

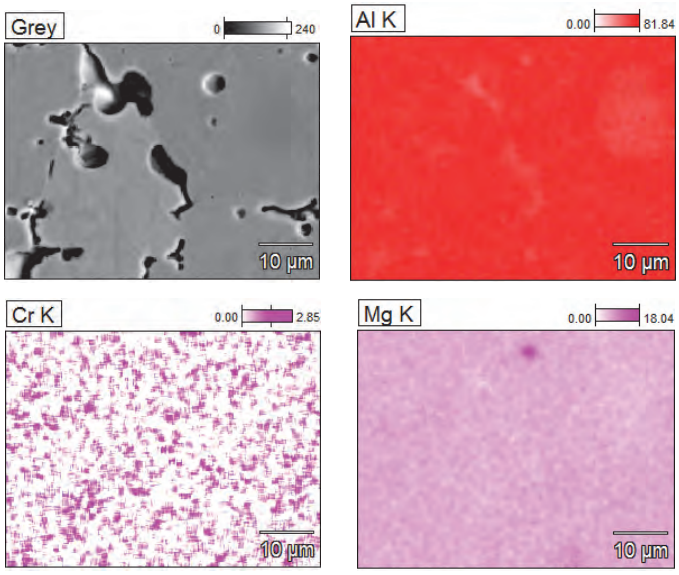

Fig. 17. Part I

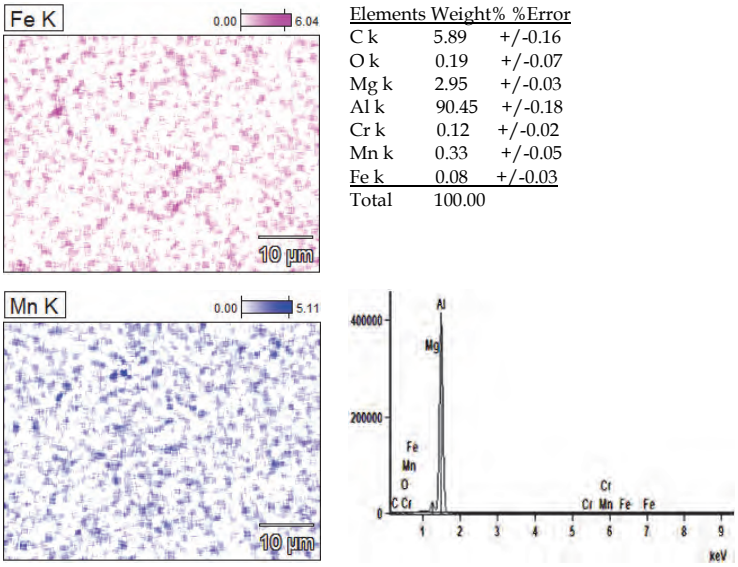

Elements	Weight%	%Error
C k	5.89	+/-0.16
O k	0.19	+/-0.07
Mg k	2.95	+/-0.03
Al k	90.45	+/-0.18
Cr k	0.12	+/-0.02
Mn k	0.33	+/-0.05
Fe k	0.08	+/-0.03
Total	100.00	

Part II

Fig. 17. Typical EM-EDS analysis of second phase particles observed in a weld performed using ER5183 filler wire.

The interdendritic component of weld metal deposited using ER4043 filler wire consisted of a fine Si-rich eutectic. Isolated Mg-rich particles are also evident (Figure 18).

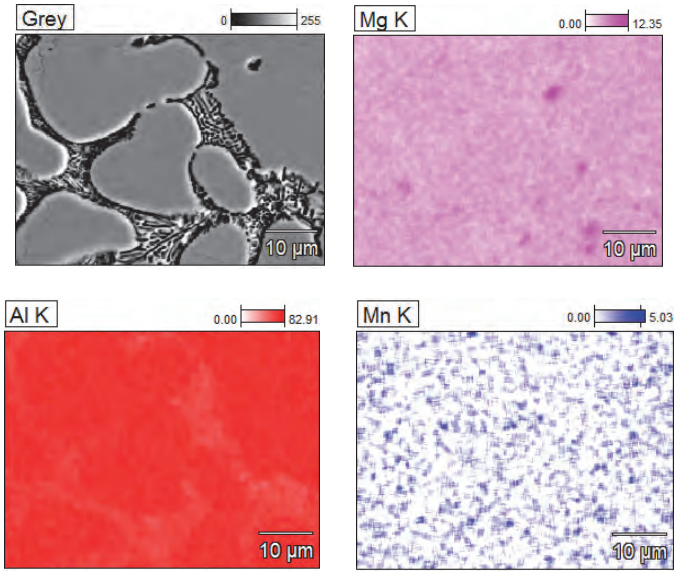

Fig. 18. Part I

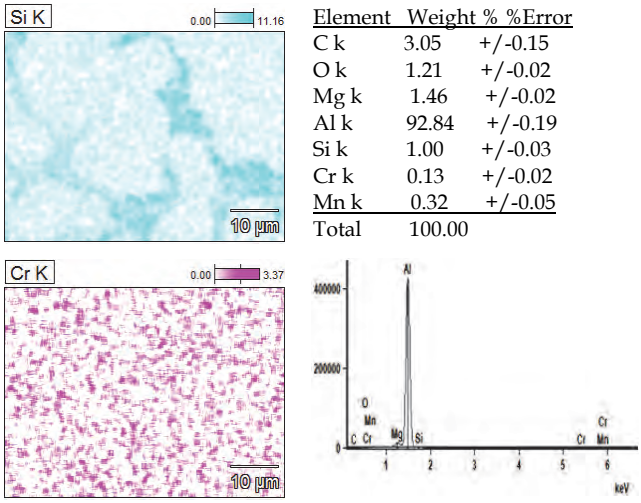

Fig. 18. Typical EM-EDS analysis of second phase particles observed in a weld performed using ER4043 filler wire.

4.2 Micro-hardness evaluation of 5083-H111 welds

The average hardness value of 5083-H111 alloy in the as-supplied condition is 91.81 HV (standard deviation of 13.20 HV) (Figure 19 and 20). Micro-hardness measurements revealed higher hardness values in the region of second-phase intermetallic particles (a maximum of about 794 HV). Figures 19 and 20 also display micro-hardness profiles across FA-GMAW welded joints performed using ER5356 and ER4043 filler wire, respectively. A similar trend was observed for the ER5183 filler metal. The lowest hardness values were observed within the weld metal of both the SA-GMAW and FA-GMAW welds produced using ER5356 or ER4043 filler wire. SA-GMAW welds displayed lower hardness values than FA-GMAW welds, regardless of the filler wire used.

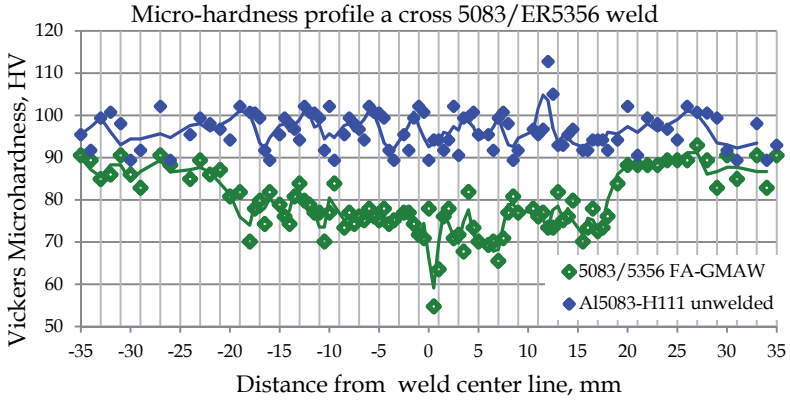

Fig. 19. Micro-hardness profile across a pulsed SA-GMAW joint welded with ER5356 filler wire.

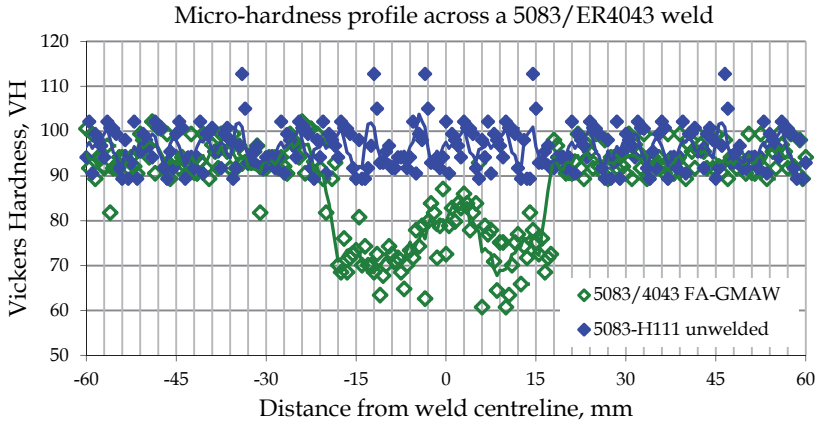

Fig. 20. Micro-hardness profile across a pulsed SA-GMAW joint welded with ER4043 filler wire.

4.3 Tensile properties of 5083-H111 aluminium

4.3.1 Tensile properties in the as-supplied condition

As shown in Figure 21, the unwelded 5083-H111 displayed moderate tensile and yield strength, and good ductility. During axial tensile testing, the crack path followed coarse second-phase particles within the matrix, as illustrated in Figure 21(a). This alloy fractured in a ductile manner, as evidenced by microvoid coalescence (dimples) observed around coarse precipitates or second-phase particles on the fracture surface (Figure 21 (b)).

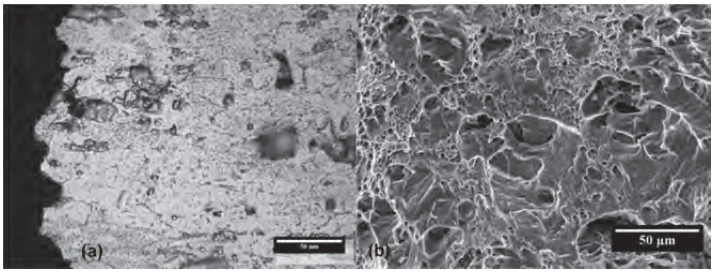

Fig. 21. Tensile fracture of the 5083-H111 as-supplied material: (a) fracture path; (b) microvoid coalescence.

4.3.2 Tensile properties of 5083-H111 welds

The transverse tensile properties of 5083 welded using ER5356, ER5183 and ER4043 filler wire are given in Figures 22 to 24, respectively. All fully dressed welds failed in the weld metal, as typically illustrated in Figures 25(a), 26 and 27. As shown in Figures 19 and 20, the hardness across welds is fairly uniform, with a moderate reduction in hardness in the weld metal. This reduction in hardness most likely prompted failure in this region during tensile testing. Any discontinuities in the weld metal, such as gas porosity or lack-of-fusion type

defects, will also affect the measured tensile properties. The ultimate tensile strength (UTS) of FA-GMAW dressed welds performed using ER5356 filler wire was very similar to that of the base metal, with ER5183 and ER4043 generally yielding lower strength values due to the inherently lower strength levels of the consumables. Figures 23 to 24 also indicate that the ultimate tensile strength (UTS) values of FA-GMAW welds are consistently higher than those of SA-GMAW welds. This can most likely be attributed to the higher incidence of porosity and welding defects observed in SA-GMAW welds (Figure 14). The strength values of fully dressed welds using ER5356 filler wire, shown in Figure 23, are significantly higher than those of undressed welds, emphasising the detrimental effect of geometrical stress concentrations (at the weld toe and root) and weld defects (such as undercut) on the measured tensile properties. Undressed welds consistently failed in the HAZ at the weld toe or root (Figure 26(c)). The tensile fractures (Figure 26) and SEM micrographs of the weld metal fracture surfaces (Figure 26) confirm a predominantly ductile failure mode in ER5356 and ER5183 welds, with mixed mode failure along the interdendritic silicon-rich eutectic regions in the ER4043 weld metal.

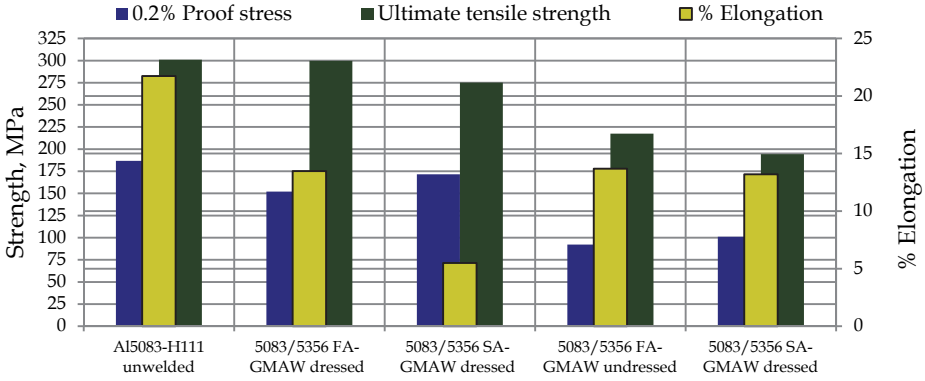

Fig. 22. Tensile Properties of 5083-H111/ER5356 welds.

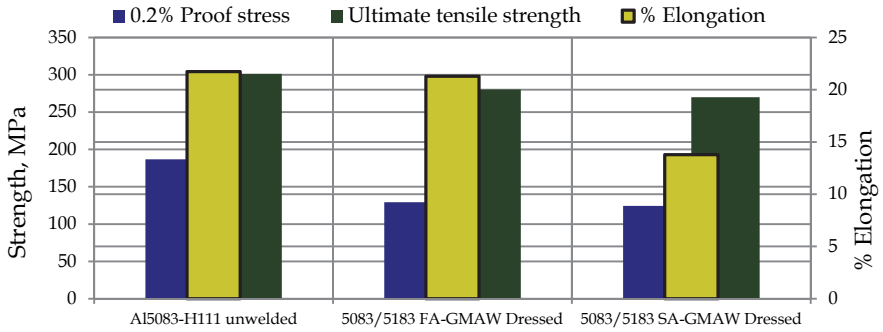

Fig. 23. Tensile Properties of 5083-H111/ER5183 welds.

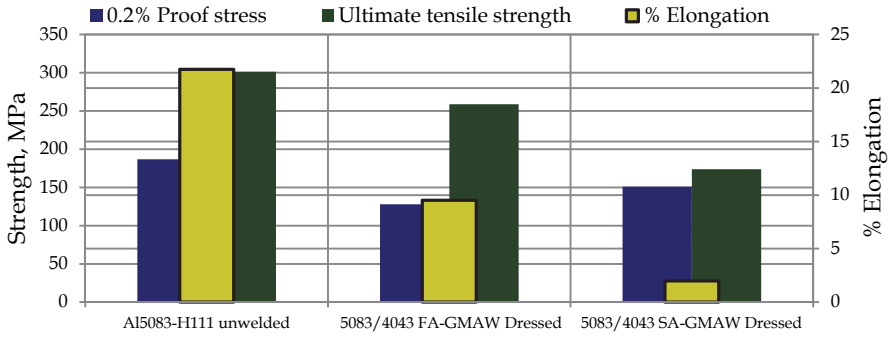

Fig. 24. Tensile Properties of 5083-H111/ER4043 welds.

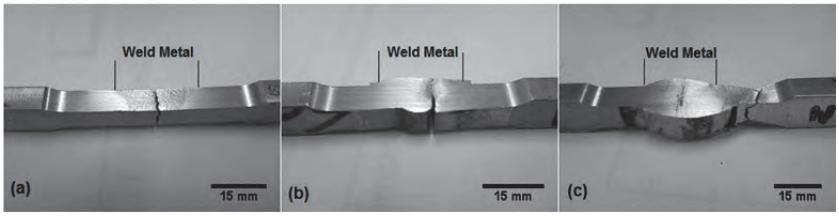

Fig. 25. Representative photographs of the tensile fractures observed in 5083 welded using ER5356, ER5183 and ER4043 filler wires: (a) fully dressed FA-GMAW weld; and (b) undressed FA-GMAW weld; and (c) undressed SA-GMAW weld.

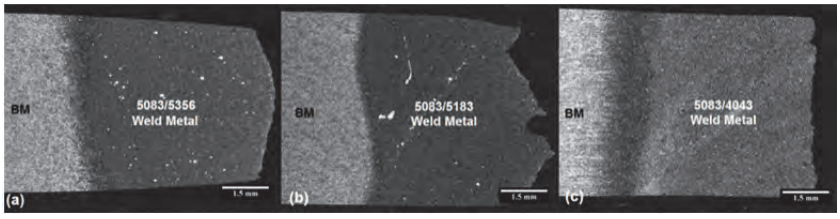

Fig. 26. Tensile fractures of weld joint in 5083 alloy welded with (a) ER5356; (b) ER5183; and (c) 4043 filler wire.

Since failure occurs preferentially in the weld metal, filler metal selection plays a significant role in determining the transverse tensile properties of the welds. ER5356 welds display tensile properties very similar to those of the unwelded base metal, with ER5183 and ER4043 providing welds with lower strength.

In the case of undressed welds, failure at the fusion line was promoted by the presence of gas pores and lack of fusion type defects at the fusion line, as shown in Figure 28.

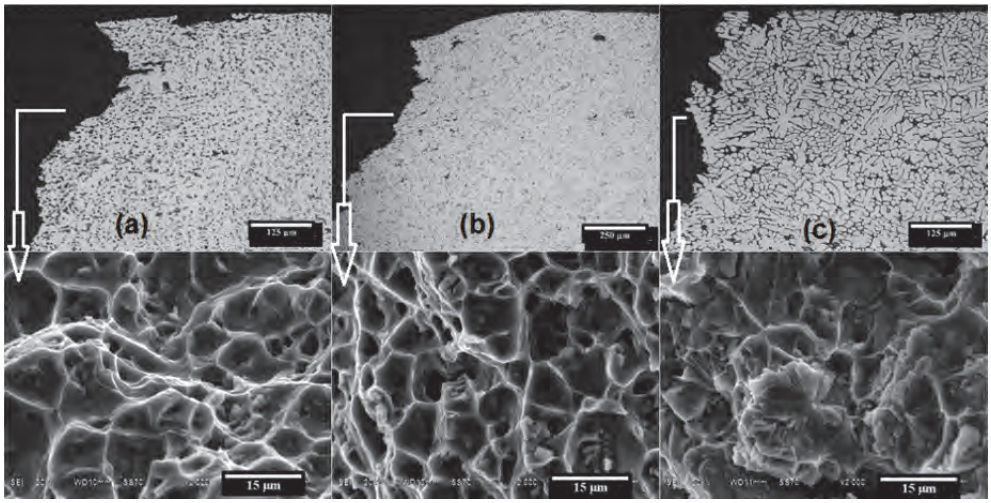

Fig. 27. Tensile fracture surfaces of fully dressed welds displaying predominantly ductile mixed-mode failure in the weld metal (a) 5083/ER5356, and (b) 5083/ER5183; and brittle failure in (c) 5083/ER4043 weld metal.

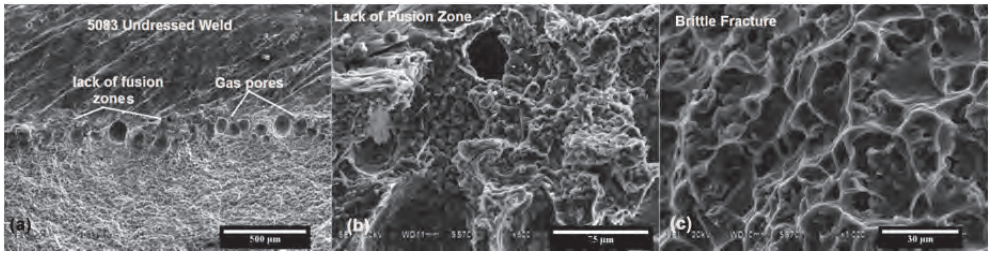

Fig. 28. Typical tensile fracture surfaces of undressed welds failing at weld/HAZ transition zone (a) lack of fusion and gas pores in weld/HAZ interface, (b) lack of fusion area; and (c) brittle mixed-mode failure in weld/HAZ interface.

4.4 Corrosion behaviour of 5083-H111 in a 3.5% NaCl solution

Aluminium 5083-H111 in the as-supplied condition exhibits pitting corrosion on immersion in 3.5% NaCl solution (maintained at a temperature of 16°C to 27°C, with a pH between 6.9 and 7.2). Typical corroded surfaces after various immersion times (with a total immersion time of 90 days) are given in Figures 29. Pitting attack is generally associated with second phase particles in the matrix (Figure 29(a)). This is consistent with the observation made on 6061-T651 aluminium alloy by K.Mutombo [27].

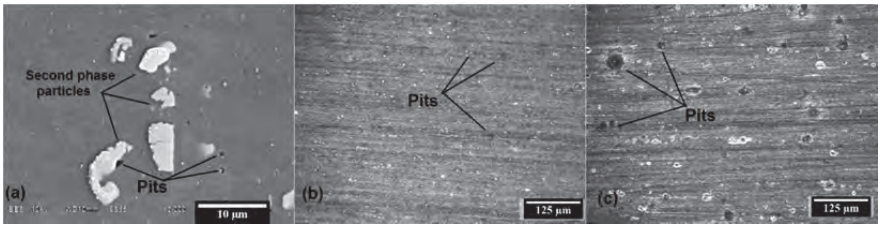

Fig. 29. Pitting corrosion observed after exposure to a 3.5% NaCl solution on the surfaces of 5083-H111 aluminium: (a) a polished surface immersed for 24 hours; (b) a ground surface immersed for 30 days; and (c) ground surface immersed for 90 days.

The pit dimensions observed on immersion of 5083-H111 in 3.5% NaCl solution are shown graphically as a function of exposure time in Figures 30. Longer exposure times increase the depth, length and width of the observed pits.

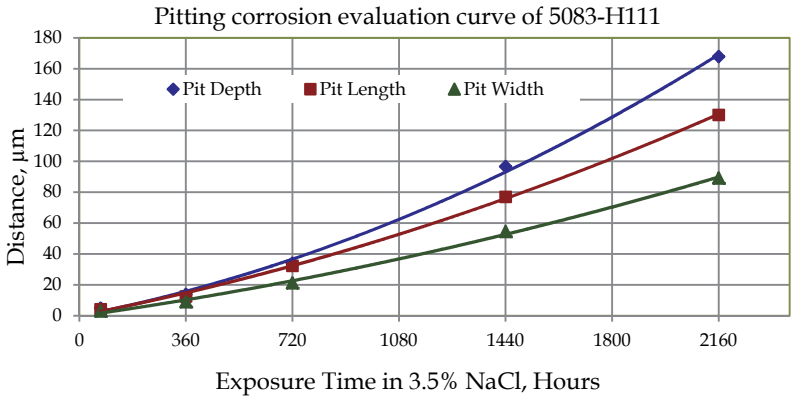

Fig. 30. Mean dimensions of pits observed in aluminium 5083-H111 exposed to 3.5% NaCl solution at temperatures between 25 and 27^0C and dissolved oxygen contents of 5.5 to 9 ppm.

Welding appeared to increase susceptibility to pitting corrosion. Welds suffered severe pitting attack on exposure to 3.5% NaCl solution. As shown in Figure 31, immersion in 3.5% NaCl solution of welds resulted in pitting of the weld metal and HAZ of ER5356 and ER5183 welds, with very severe corrosive attack of the ER4043 weld metal and HAZ.

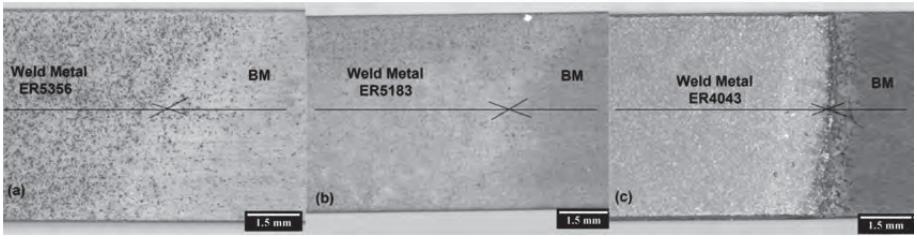

Fig. 31. Typical corrosion of welds after free immersion in 3.5% NaCl solution for 60 days: (a) ER5356; (b) ER5183; (c) ER4043 filler wire.

4.5 Fatigue properties of 5083-H111 in the as-supplied condition

4.5.1 Fatigue properties in the as-supplied condition

S-N_f curves of 5083-H111 in the as-supplied condition after testing in air and in 3.5% NaCl solution are shown in Figure 32. As expected, the number of cycles to failure increases with a decrease in the applied stress amplitude (Sa). The unwelded aluminium 5083-H111 displayed considerably longer fatigue life in air than in 3.5% NaCl solution, especially at higher stress amplitudes.

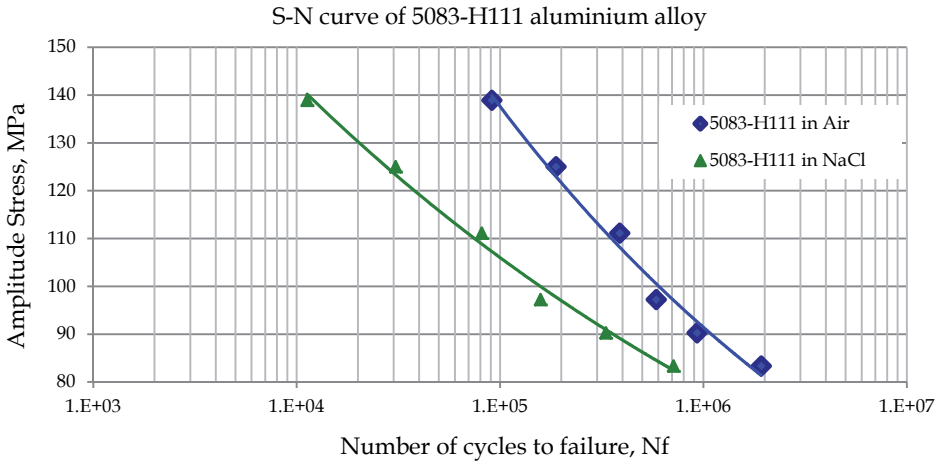

Fig. 32. S-N curves of 5083-H111 aluminium in the as-supplied condition.

During testing in air, fatigue cracks initiated preferentially at the free surfaces of the sample at discontinuities such as slip lines, polishing or machining marks and precipitates or inclusions. This is illustrated in Figure 33(a) to (c). Once initiated at the free surface (at inclusions (Figure 33(a) and (b)), the cracks propagated rapidly during testing, followed by final ductile failure when the remaining cross section of the sample could no longer sustain the applied stress.

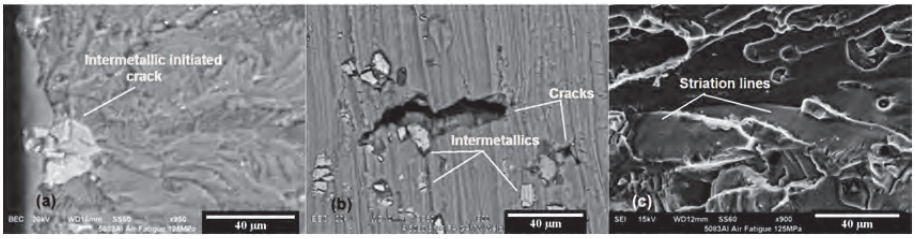

Fig. 33. (a) Surface crack initiation at second phase particles; (b) crack initiation due to disbonding between precipitates and the matrix; and (c) crack propagation.

Immersion in 3.5% NaCl solution during fatigue testing shortened the fatigue life significantly. As shown in Figure 34, crack initiation was accelerated by the presence of corrosion pits at the surface of the samples. These pits formed preferentially at precipitates or inclusions due to the galvanic effect between the particle and the aluminium matrix.

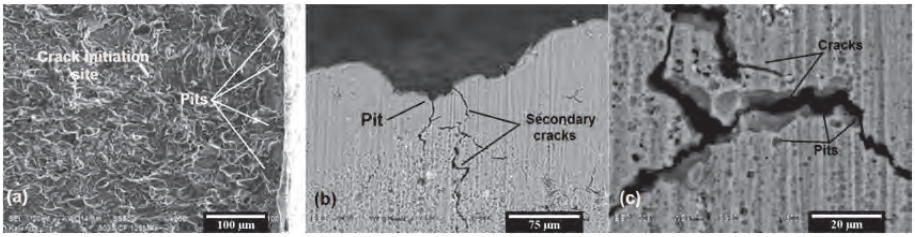

Fig. 34. (a) Multiple fatigue crack initiation at small corrosion pits; (b) crack propagation from corrosion pits; and (c) fatigue crack associated with small pits.

The fatigue damage ratio (DR) is the ratio between the number of cycles to failure in 3.5% NaCl solution ($N_{f\ NaCl}$) and the number of cycles to failure in air ($N_{f\ Air}$), as shown in equation (5).

$$DR = \frac{N_{fNaCl}}{N_{fAir}} \tag{5}$$

The limit values of the fatigue damage ration are zero (0) and one (1). The DR approaches zero only when $N_{f\ NaCl}$ approaches zero, i.e. pitting corrosion is the dominant process in determining the corrosion fatigue behaviour. Corrosion pits act as stress raisers by rapidly initiating fatigue cracks. When DR approaches one, or $N_{f\ NaCl}$ approaches $N_{f\ Air}$, the dominant process determining fatigue life is the fluctuating stress.

The fatigue damage ratios (DR) of 5083-H111 aluminium in the as-supplied condition are shown graphically in Figure 35. This graph indicates that the effect of pitting corrosion on fatigue properties in unwelded specimens is most pronounced at higher stress amplitudes. At high stress levels, corrosion pits act as sharp stress raisers, accelerating fatigue crack initiation. The effect of the corrosive environment on fatigue properties becomes less apparent at lower stress amplitudes, but is unlikely to approach a ratio of one (signifying that the corrosive environment has no influence on fatigue behaviour).

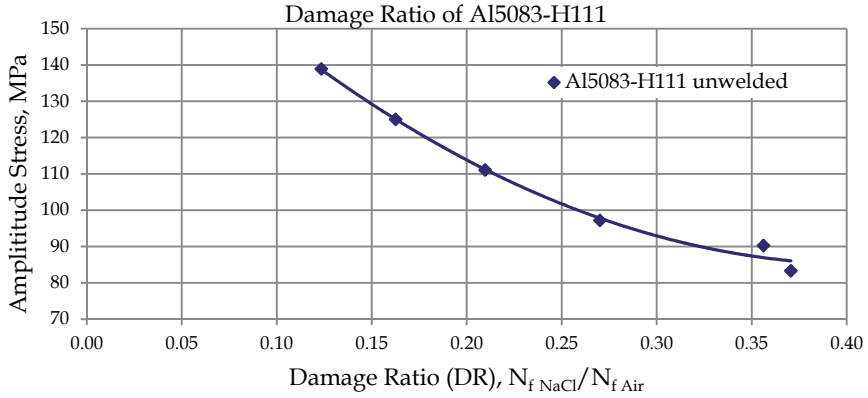

Fig. 35. Fatigue damage ratio (DR) of 5083-H111 aluminium.

4.5.2 Fatigue behaviour of 5083-H111 aluminium welds

4.5.2.1 Aluminium 5083-H11 welded using ER5356 filler wire

The results of fatigue tests in air of 5083 aluminium joined using ER5356 filler wire are shown in Figure 36. The data points shown represent median values, whereas the S-N_f curves were fit using the power law. It is evident that welding reduces the fatigue life significantly. SA-GMAW welds (fully dressed and as-welded) and as-welded (undressed) FA-GMAW welds display similar fatigue properties, with the fully dressed SA-GMAW welds performing marginally better than the undressed joints. The dressed FA-GMAW welds display much higher fatigue properties, which can be attributed to the absence of sharp stress concentrations at the weld toe and root, and the reduced incidence of welding defects such as porosity.

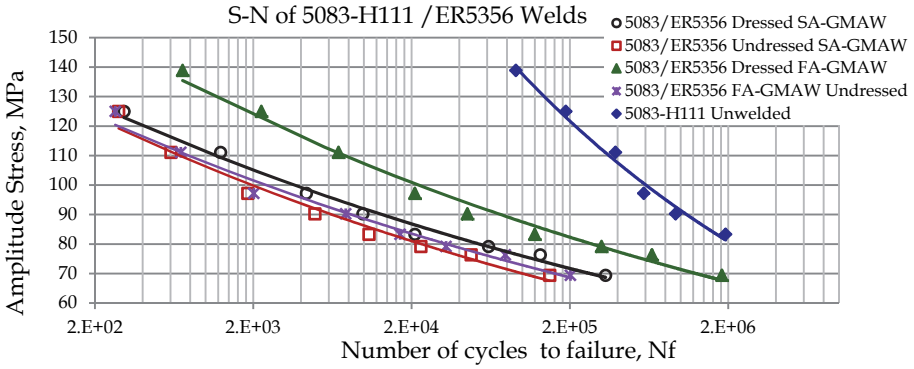

Fig. 36. Fatigue properties of 5083 welded with ER5356, tested in air.

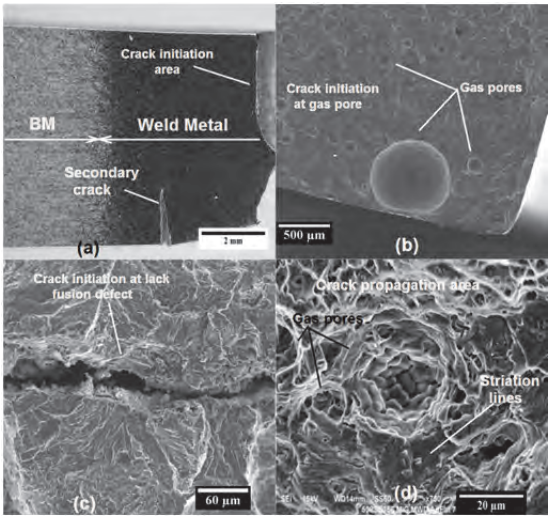

Fig. 37. Typical fatigue fractures in 5083 welds (a) crack initiation in the weld metal; (b) crack initiation associated with a large gas pore; (c) crack initiation at a lack-of-fusion type defect; (d) crack propagation associated with gas pores.

Fatigue cracks initiated preferentially at gas pores, lack-of-fusion type defects and incomplete weld penetration; and at the weld toes of undressed joints (Figure 37). Crack propagation occurred preferentially in the weld metal.
The results of fatigue tests of 5083 joined using ER5356 filler wire in 3.5% NaCl solution are shown in Figure 38. The results indicate that immersion in NaCl during fatigue testing reduces the fatigue properties of both the SA-GMAW and FA-GMAW welds. The advantage gained by FA-GMAW in reducing the number of welding defects are largely negated in the presence of a corrosive environment due to the introduction of corrosion pits as preferential crack initiation sites. The FA-GMAW weld therefore displays similar fatigue performance to the SA-GMAW weld under corrosion fatigue conditions.

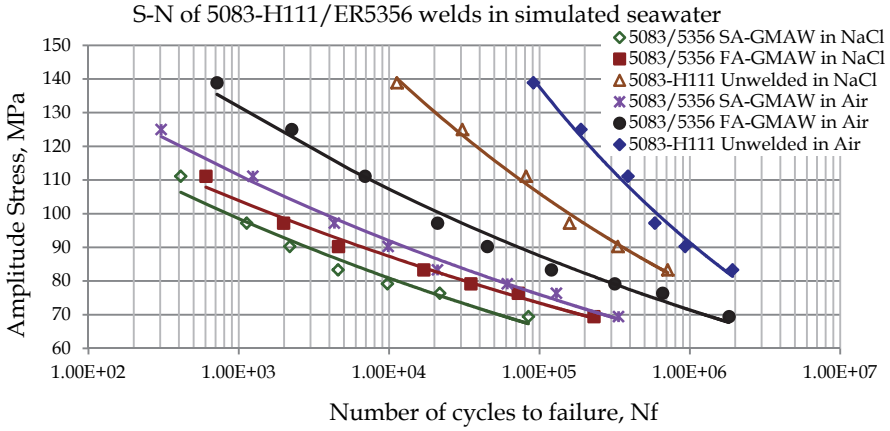

Fig. 38. Fatigue properties of 5083 welded with ER5356, tested in 3.5% NaCl solution.

The fatigue damage ratio (DR) curve of 5083/ER5356 welds shown in Figure 39 reveals that the effect of pitting corrosion on fatigue properties is most pronounced at stress amplitudes between 80 and 70 MPa.

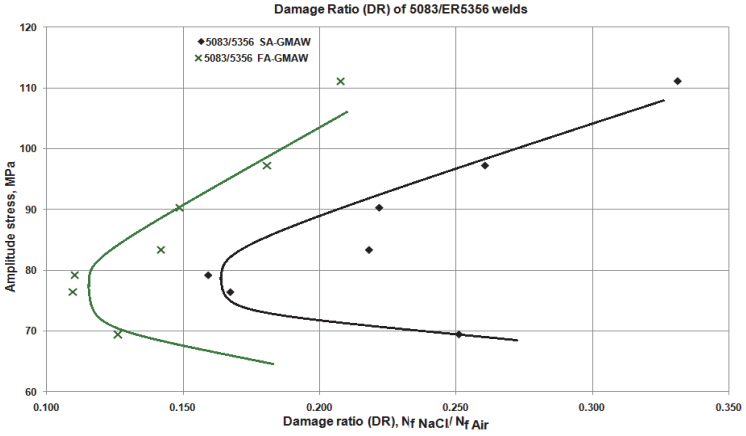

Fig. 39. Fatigue damage ratio of 5083 aluminium welded with ER5356 filler metal.

In this stress range, pits act as sharp stress raisers, accelerating fatigue crack initiation. Due to the presence of pre-existing weld defects, the effect of the corrosive environment on the fatigue properties of the welds becomes less apparent at higher stress amplitudes. At these higher stress amplitude values, the number of cycles to failure decreases and the effect of pitting corrosion becomes less apparent.
During fatigue testing in 3.5% NaCl solution, cracks initiate preferentially at pits in the weld metal (Figure 40(a) and (b)), or at discontinuities such as the lack-of-fusion type defect shown in Figure 40(d)).

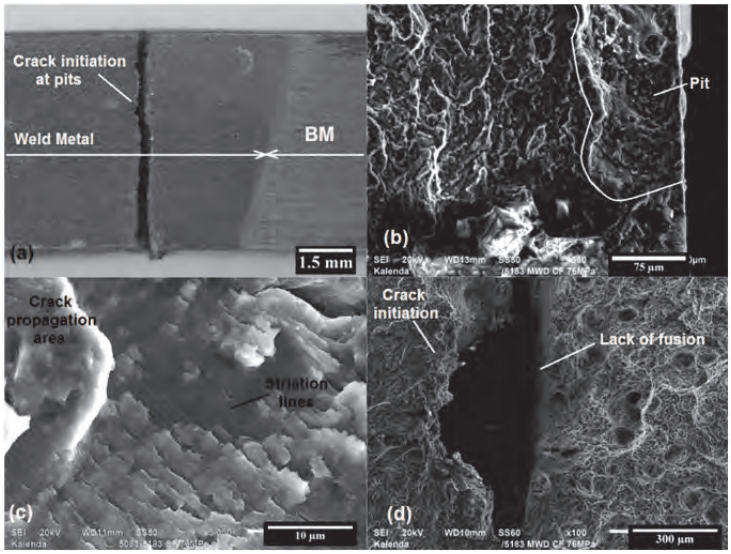

Fig. 40. Typical features of fatigue fracture in 5083/ER5356 welds tested in 3.5% NaCl: (a) and (b) crack initiation at pits in the weld metal; (c) crack propagation in the weld metal; and (d) crack initiation at a lack-of-fusion type defect.

4.5.2.2 Aluminium 5083-H111 welded using ER5356 filler wire

The fatigue properties of 5083-H111 aluminium welded with ER5183 filler wire using SA-GMAW or FA-GMAW are presented in Figure 41. Welding reduces the fatigue life tested in air considerably. Failure occurs in the weld metal, which has a lower hardness and strength than the base materials (as shown in Figures 20 to 21 and 23 to 25). Cracks initiate preferentially at weld defects such as gas pores, lack-of-fusion type defects, incomplete penetration and slag inclusions. The 3.5% NaCl corrosive environment reduces the number of cycles to failure for SA-GMAW and FA-GMAW welds. Cracking occurs preferentially in the softer weld metal which corrodes faster than the base material (Figure 40(a)). Crack initiation is accelerated by pits that formed prematurely in the weld metal at defects such as gas pores, lack-of-fusion defects and slag inclusions. Very little difference is evident between SA-GMAW and FA-GMAW welds, suggesting that the lower defect content of the automatic welds does not affect the fatigue behaviour significantly.

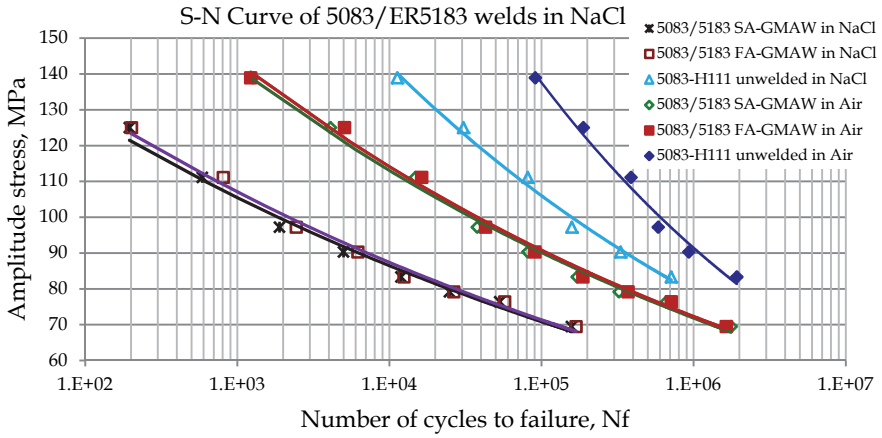

Fig. 41. Fatigue properties of Al5083/ER5183 welds tested in air and 3.5% NaCl solution.

The fatigue damage ratio of aluminium 5083 welded with ER5183 filler wire is shown in Figure 43 for SA-GMAW and FA-GMAW welds. Corrosion fatigue plays a more dominant role at higher stress amplitudes, where the presence of welding defects may accelerate pitting corrosion, leading to rapid fatigue crack initiation and propagation.

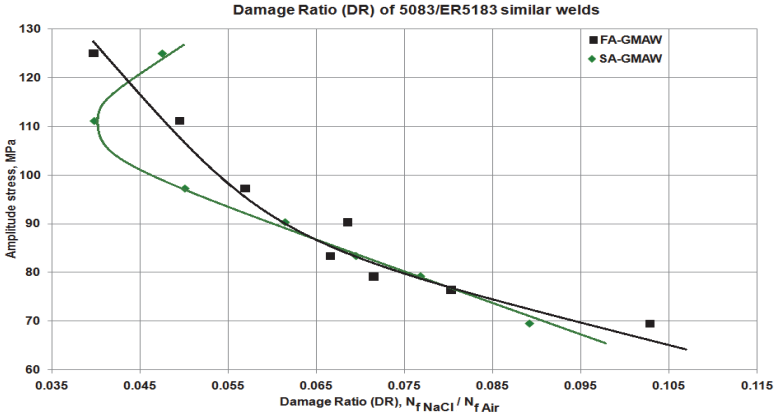

Fig. 42. Fatigue damage ratio of 5083-H111 welded with ER5183 filler wire.

4.5.2.3 Aluminium 5083-H111 welded using ER4043 filler wire

Figure 43 displays the fatigue properties of aluminium alloy 5083-H111 welded with ER4043 filler wire using SA-GMAW and FA-GMAW. Failure occurs in the weld metal and these welds exhibit reduced fatigue life compared to that of unwelded 5083-H111 tested in air. The 5083/ER4043 welds appear to be sensitive to the presence of weld defects, with the SA-GMAW welds displaying lower fatigue properties than the FA-GMAW welds. The SA-GMAW and FA-GMAW welds display similar corrosion fatigue life when tested in 3.5% NaCl salt water environment, suggesting that the presence of a higher percentage of welding defects in the SA-GMAW welds did not affect the fatigue behaviour in the

corrosive environment to any significant extent. The short fatigue life of these welds can be attributed to the poor corrosion resistance of the ER4043 welds. Pit formation is rapid, with fatigue cracks initiating prematurely at corrosion pits.

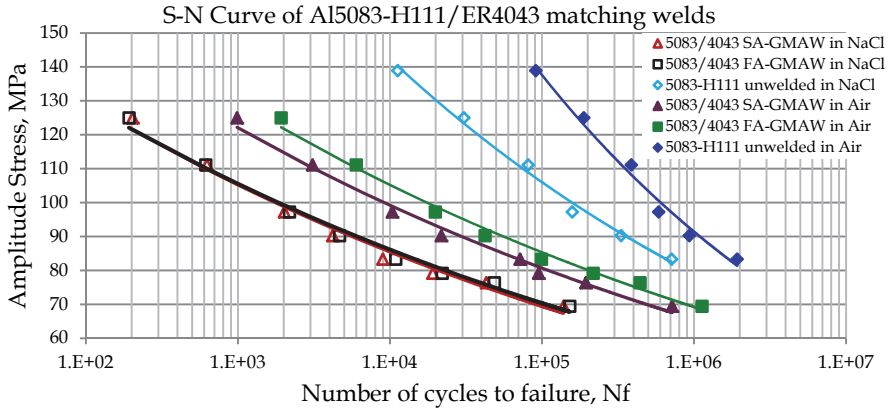

Fig. 43. Fatigue properties of 5083 aluminium welded with ER4043 filler metal.

The fatigue damage ratio (DR) values of 5083 aluminium, welded using ER4043 filler metal, are presented in Figure 44. The fatigue ratio values are low, suggesting that the fatigue properties of the welds are sensitive to pitting corrosion in the NaCl solution. The FA-GMAW welds appear to be affected to a greater extent by the presence of a corrosive environment. These welds displayed slightly better fatigue properties than the SA-GMAW welds in air, probably due to the lower number of weld defects. In the NaCl solution, however, both curves shift to lower numbers of cycles to failure, with the fully automatic curve shifting more than the semi-automatic curve. This suggests that the availability of welding defects ceases to dominate the fatigue behaviour, with crack initiation at corrosion pits becoming controlling. The rapid pitting rate of the ER4043 weld in NaCl therefore creates large numbers of potential pit initiation sites in both the FA-GMAW and SA-GMAW welds, resulting in a very low damage ratio, especially for the FA-GMAW welds.

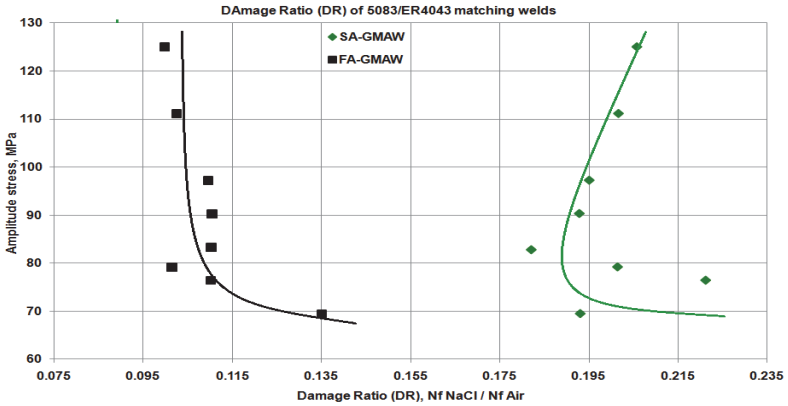

Fig. 44. Fatigue damage ratio of 5083/ ER4043 welds.

The results presented in this study confirm that the fatigue properties of 5083-H111 aluminium are adversely affected by welding. Fatigue cracks preferentially initiated at the stress concentration caused by the weld toes or the weld root (in as welded joints) or the weld metal at defects such as gas pores, lack-of-fusion type defects and incomplete weld penetration. Fatigue failure was accelerated by the presence of a corrosive environment due to the formation of corrosion pits.
The influence of filler metal selection on the mechanical properties of the welds is discussed below.

4.5.3 Effect of filler wire selection on the mechanical properties of 5083-H111 aluminium welds

The influence of filler metal selection (ER4043, ER5183 or ER5356) on the transverse tensile properties of welds in 5083-H111 aluminium is shown in Figure 45. The tensile strength of 5083 alloy welded with ER5356 is similar to that of the base metal, but the ductility is considerably lower. Welds performed using ER5183 filler wire display excellent ductility, good tensile strength, but low yield stress, whereas welds performed using ER4043 filler metal display poor strength and ductility.

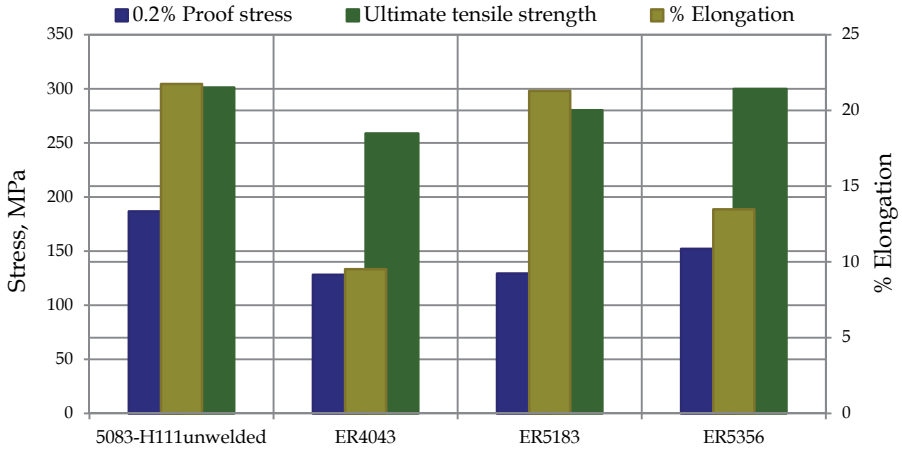

Fig. 45. Tensile properties of dressed welds in 5083-H111 aluminium joined using ER4043, ER5183 and ER5356 filler wires (pulsed GMAW).

Figure 46 presents the fatigue properties of 5083-H111 welded using ER4043, ER5183 and ER5356 filler metals. Although the fatigue properties are very similar, the weld performed using ER5183 filler wire displays slightly longer fatigue life in air. The good fatigue resistance of the ER5183 welds in air can probably be attributed to a good combination of

high strength and excellent ductility. Exposure to a corrosive medium during fatigue testing reduced the fatigue life significantly, but despite the observed differences in mechanical properties, filler metal selection had very little effect on the corrosion fatigue properties. All three welds displayed similar corrosion fatigue properties during testing in 3.5% NaCl solution.

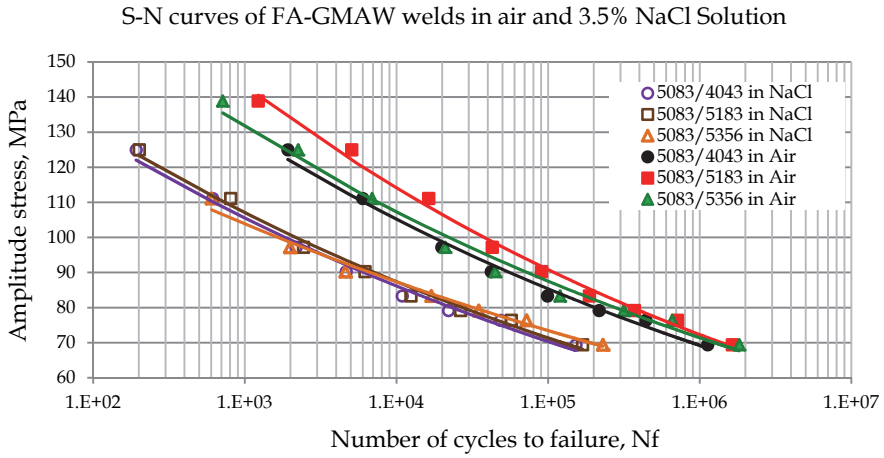

Fig. 46. Fatigue properties of FA-GMAW welds in 5083-H111 welded with ER4043, or ER5183, or ER5356 filler wire.

The results described above indicate that ER5356 or ER5183 filler metal is recommended for joining this alloy, with ER5356 yielding high strength welds and ER5183 providing a good combination of high strength and excellent ductility. Fully automatic welding, with its good control over weld dimensions and its lower defect content, ensures optimal resistance to fatigue failure.

5. Conclusions and recommendations

Both semi-automatic and fully-automatic welding reduces the strength and hardness of the Al5083-H111 welds produced with ER5356, ER5183 and ER4043 filler wires. This loss in strength and hardness was more pronounced in the semi-automatic gas metal arc welds. Lower hardness was revealed in the centre line of welds.

The fatigue lives were severely reduced in the undressed welds due to the severe stress concentration presented by the weld toes. Dressing of the welds improved the fatigue properties significantly. As a result of improved control over weld profile, fully-automatic welds consistently outperformed semi-automatic welds. Fatigue cracks initiated at gas pores, lack of fusion defects, incomplete weld penetration and weld toes. The presence of a corrosive environment accelerated the fatigue failure due to the formation of corrosion pits that initiated preferentially at weld defects or coarse second phase particles and facilitated rapid fatigue crack initiation.

ER5356 or ER5183 filler metal is recommended for joining 5083 aluminium alloys, with ER5356 yielding high strength welds and ER5183 providing a good combination of high strength and excellent ductility. Fully automatic welding, with ensures optimal resistance to fatigue failure.

6. Acknowledgements

My sincere thanks to the Light Metals Development Network and the THRIP programme for financial support during this investigation.
I would also like to express my appreciation to Professor Madeleine du Toit for her support and guidance. The contribution and technical advice of Professor Waldo Stumpf, Professor Chris Pistorius and Dr Tony Paterson are also gratefully acknowledged.
Finally the technical support of Willie Du Preez, Sagren Govender, Chris McDuling and Erich Guldenpfennig from the Council for Scientific and Industrial Research (CSIR) is gratefully acknowledged.

7. References

[1] Lean, P.P.; Gil, L. & Ureña, A. (2003). Dissimilar welds between unreinforced AA6082 and AA6092/SiC/25p composite by pulsed-MIG arc welding using unreinforced filler alloys (Al–5Mg and Al–5Si), *J.Mat.Pro.Tec.*, vol. 143-144, pp. 846-850

[2] Czechowski, M. (2004). Corrosion Fatigue of GMA Al-Mg Alloy, *Advances in Materials Science,* vol. 4, No. 2004, pp. 16-24.

[3] Praveen, P. & Yarlagadda, P.K.D.V. (2005). Meeting challenges in welding of aluminium alloys through pulse gas metal arc welding, *J.Mat.Proc.Tec.,* vol. 164-165, pp. 1106-1112

[4] Olson, D.L.; Siewert, T.A.; Liu, S.; Edwards, G.R. 2007, *Welding, Brazing, and Soldering*, ASM International, USA

[5] Wilcox, D.V.; Adkins, H.; Dickerson, P.B.; Hasemeyer, E.A. & Lockwood, L. (1972). Welding Aluminum, In: *Welding Aluminum*, 6th edn, American welding society, Florida, pp. 69.2-69.4-69.25

[6] Maddox, S.J. (1991). Fatigue Strength of Welded Structures, In: *Fatigue Strength of Welded Structures*, 2nd edn, Abington Publishing, Cambrige, England, pp. 19-27-30-36, 38-43, 66-70

[7] Jones, D.A. (1996). Principals and Prevention of CORROSION, In: *Principals and Prevention of CORROSION*, 2nd edn, Prentice-Hall, Inc., United States of America, pp. 200-200-220, 236-247, 262-263, 279-285, 307, 309-316, 322

[8] Vargel, C. (2004). Corrosion of Aluminum, In: *Corrosion of Aluminum* Elsevier, London, pp. 92-96-97, 124

[9] Maggiolino, S. & Schmid, C. (2008). Corrosion resistance in FSW and in MIG welding techniques of AA6XXX, *J.Mat.Proc.Tec.,* vol. 197, no. 1-3, pp. 237-240

[10] Cramer, S.D.; Covino, B.S. (2003). *Corrosion: Fundamentals, Testing, and Protection*, ASM International, USA

[11] Winkler, S.L.; Ryan, M.P. & Flower, H.M. (2004). Pitting corrosion in cast 7XXX aluminium alloys and fibre reinforced MMCs, *Corrosion Science,* vol. 46, no. 4, pp. 893-902

[12] Hatch, J.E. (1984) Aluminium: Properties and Physical Metallurgy In: *Aluminium: Properties and Physical Metallurgy* American Society for Metals, USA, pp. 242-242-248, 253.

[13] ASTM International. (2004). *Standard Test Method for Vickers Hardness of Metallic of Materials*, ASTM international, West Conshohocken

[14] Davis, J.R. (1998). *Aluminum and Aluminum Alloys*, 4th edn, ASM International, USA

[15] Geoffroy, N.; Vittecoq, E.; Birr, A.; de Mestral, F. & Martin, J. (2007). Fatigue behaviour of an arc welded Al–Si–Mg Alloy, *Scripta Materialia,* vol. 57, no. 4, pp. 349-352

[16] Ishihara, S.; Saka, S.; Nan, Z.Y.; Goshima, T. & Sunada, S. (2006). Prediction of corrosion fatigue lives of aluminium alloy on the basis of corrosion pit growth law, *Fatigue and Fracture of Engineering Materials and Structures,* vol. 29, no. 6, pp. 472-480

[17] ASM International. (2007). *Fatigue and Fracture*, ASM International, USA

[18] Pidaparti, R.M. & Rao, A.S. (2008). Analysis of pits induced stresses due to metal corrosion, *Corrosion Science,* vol. 50, no. 7, pp. 1932-1938

[19] Chlistovsky, R.M.; Heffernan, P.J. & DuQuesnay, D.L. (2007). Corrosion-fatigue behaviour of 7075-T651 aluminum alloy subjected to periodic overloads, *I.J.Fatigue,* vol. 29, no. 9-11, pp. 1941-1949

[20] Chen, G.S.; Wan, K.; Gao, M.; Wei, R.P. & Flournoy, T.H. (1996). Transition from pitting to fatigue crack growth—modeling of corrosion fatigue crack nucleation in a 2024-T3 aluminum alloy, *Materials Science and Engineering A,* vol. 219, no. 1-2, pp. 126-132

[21] ASTM International. (2002). Standard Test Method for Macroetching Metals and Alloys, ASTM International, West Conshohocken

[22] ASTM International. (2001). Standard Guide for Metallographic Specimens, ASTM International, West Conshohocken.

[23] ASTM International. (2002). Standard Test Method for Microindentation Hardness of Materials, ASTM International, West Conshohocken.

[24] ASTM International. (2004). Standard Test Methods for Tension Testing of Metallic Materials, ASTM International, West Conshohocken.

[25] ASTM International. (2004). Standard Practice for Laboratory Immersion Corrosion Testing of Metals, ASTM International, West Conshohocken.

[26] ASTM International. (1999). Standard Guide for Examination and Evaluation of Pitting Corrosion, ASTM International, West Conshohocken

[27] ASTM International. (2002). Standard Practice for Conducting Force Controlled Constant Amplitude Axial Fatigue Test of Metallic Materials, ASTM International, West Conshohocken

[28] Mutombo, K. (2011). Intermetallic Particles-Induced Pitting Corrosion in 6061-T651 Aluminium Alloy, *Materials Science Forum,* vol. 690, no. 2011, pp. 389-392